Geophys. J. Int. (2003) **153,** 27–51

Evolution of orogenic wedges and continental plateaux: insights from crustal thermal–mechanical models overlying subducting mantle lithosphere

O. Vanderhaeghe,[1,2,*] S. Medvedev,[1] P. Fullsack,[1] C. Beaumont[1] and R. A. Jamieson[2]

[1]*Department of Oceanography, Dalhousie University, Halifax, Nova Scotia, Canada,* B3H 4J1. *E-mails: olivier.vanderhaeghe@g2r.uhp-nancy.fr; sergei@adder.ocean.dal.ca; philippe@adder.ocean.dal.ca; chris.beaumont@dal.ca; beckyj@is.dal.ca*

[2]*Department of Earth Sciences, Dalhousie University, Halifax, Nova Scotia, Canada,* B3H 3J5

Accepted 2002 August 20. Received 2002 July 17; in original form 2001 July 9

SUMMARY

The links between an early phase of orogenesis, when orogens are commonly wedge shaped, and a later phase, with a plateau geometry, are investigated using coupled thermal–mechanical models with uniform velocity subduction boundary conditions applied to the base of the crust, and simple frictional–plastic and viscous rheologies. Models in which rheological properties do not change with depth or temperature are characterized by growth of back-to-back wedges above the subduction zone. Wedge taper is inversely dependent on the Ramberg number (Rm; gravity stress/basal traction); increasing convergence velocity or crustal strength produces narrower and thicker wedges. Models that are characterized by a decrease in crustal viscosity from η_c to η_b with depth or temperature, leading to partial or full basal decoupling of the crust from the mantle, display more complex behaviour. For models with a moderate viscosity ratio, $\eta_b/\eta_c \sim 10^{-1}$, the crustal wedges have dual tapers with a lower taper in the central region and a higher taper at the edges of the deformed crust. A reduction in the viscosity ratio ($\eta_b/\eta_c \sim 10^{-2}$) is sufficient to cause a transition of the central wedge region to a plateau. This transition depends on the basal traction, therefore the thickness of the weak basal layer also affects the transition. Further reduction of the viscosity ratio ($\eta_b/\eta_c \sim 10^{-4}$) leads to full basal decoupling and the development of plateaux in all cases considered. In most models, the plateaux grow laterally at constant thickness between characteristic edge peaks associated with the transitions from coupled to decoupled lower crust. Where the crust is fully decoupled, large-scale model geometries for both depth- and temperature-dependent rheologies are similar with gravity-driven flow concentrated in the low-viscosity region. However, strong lateral temperature gradients within these models, controlled by the interaction of horizontal and vertical thermal advection, diffusion and heterogeneous thickening of the radioactive crustal layer, lead to differences in the velocity and deformation fields between the two cases, particularly at the plateau margins. The results suggest that simple depth-dependent viscosity models may be reasonable approximations for describing the large-scale geometry of fully developed plateaux, but that they are not appropriate for describing the internal features of large orogenic systems or the transition from wedge to plateau geometry.

Key words: continental deformation, crustal deformation, isostasy, orogeny, radioactivity, topography, viscosity.

1 INTRODUCTION

Orogenic belts are zones of thickened continental crust that form as a result of convergence between lithospheric plates. The dynamic evolution of an orogen is controlled by the thermal and mechanical evolution of the zone of thickened crust and underlying mantle, and by interactions between gravitational, compressional and basal traction forces. Various approaches have been used to investigate these factors. 1- and 2-D thermal-kinematic models (England & Thompson 1984; Henry *et al.* 1997; Huerta *et al.* 1996; Thompson & Connolly 1995) have revealed the effect of radioactive heat production in thickened crust on the thermal evolution of model

*Now at Université Henri Poincaré Nancy 1, UMR 7566 G2R, Géologie et Gestion des Ressources Minérales et Energétiques, BP 239, 54506 Vandoeuvre-lès-Nancy Cedex, France.

orogens, and the importance of thermal weakening on the integrated strength of the lithosphere (Sonder *et al.* 1987). Models designed to understand the mechanics of orogenic belts have included rheologies ranging from uniform–plastic or frictional–plastic (Chapple 1978; Dahlen *et al.* 1984; Davis *et al.* 1983; Willett *et al.* 1993) to viscous (Bird 1991; Buck & Sokoutis 1994; Ellis *et al.* 1995; England & McKenzie 1982; Houseman & England 1986; Houseman *et al.* 1981; Royden 1996; Willett 1999; Shen *et al.* 2001). More recently, 2-D coupled thermal–mechanical models have been used to investigate dynamic interactions between heat and tectonics in orogenic systems (Batt & Braun 1997; Jamieson *et al.* 1998).

The purpose of this paper is to investigate the links between early phases of orogenesis, when orogens commonly have a wedge shaped cross-section geometry (e.g. Alps, Southern Alps (NZ), Pyrenees, and Taiwan), and a later phase when plateaux may develop (e.g. Tibet and the Andes Altiplano). This problem has previously been approached both in the context of distributed whole lithosphere deformation (for example, England & McKenzie 1982; England & Houseman 1988; Bird 1989) and in the context of underthrusting/subduction of the mantle lithosphere beneath crust that undergoes distributed deformation (e.g. Willett *et al.* 1993; Royden 1996; Jamieson *et al.* 1998; Shen *et al.* 2001). Here we focus on the subduction model and show how mechanical and thermo–mechanical evolution of the overlying crust can explain these two phases of orogenesis. We also investigate which properties of the evolving model orogen determine the characteristics of the two phases and what determines the transition between them. Specifically, we test whether prolonged thickening of the crust during orogenesis followed by decoupling of the crust from the mantle, as the temperature rises from accumulated radioactive heating, can account for the transition from the wedge to plateau phase. The results allow the predictions of models with simple temperature- and depth-dependence of viscosity and driven by mantle subduction to be compared and contrasted with those based on distributed deformation of the whole lithosphere.

Section 2 describes the basic assumptions incorporated into the model that we investigate. It outlines the first-order force balance and the thermal controls on the two end-member phases, wedge and plateau. In addition to defining the problem this section provides framework for the interpretation of the model results. In Sections 3, 4 and 5 a coupled thermal–mechanical model is used to investigate numerically the corresponding evolution of orogenic crust subject to subduction of the underlying mantle lithosphere. In keeping with the conceptual model, the numerical model properties are purposely kept simple in order to isolate the changing roles of the component forces that control the crust as it thickens, and as the temperature and rheology evolve. In particular, a comparison is made between models that have depth-dependent and thermally dependent rheologies.

2 DESCRIPTION OF THE PHYSICAL MODEL

Plane-strain model orogens in which lithospheric convergence is accommodated by crustal shortening and thickening and by subduction of the underlying mantle lithosphere can be described to first order using the concepts shown in Figs 1 and 2. We outline two simple end-member cases: (1) the crust has uniform linear–viscous properties with a strong base (Fig. 1a) and; (2) the crust has a layered viscous rheology in which the basal layer is weak (Fig. 1b). We interpret these cases to correspond to two phases of orogenesis, the first, the 'wedge' phase, when the lower crust is cold, and the second, the 'plateau' phase, when the lower crust becomes increasingly hot as a result of crustal thickening.

The first orogenic case is characterized by the growth of back-to-back tectonic wedges above the subduction zone (Fig. 1a, see caption for details). Following Medvedev (2002) we analyse the horizontal balance of forces acting on the pro-wedge:

$$F_g + F_c - F_t = 0 \tag{1}$$

The influence of gravity, F_g, is estimated from the vertically integrated lateral variation in lithostatic pressure and is non-zero when the crustal thickness varies laterally. The basal traction force, F_t, is the integral of the basal shear stress along the base. The compressive force, F_c, is estimated by integrating the horizontal normal stress over the crustal thickness. Note that F_g and F_c have the same sign. Both oppose the basal traction, which is the primary source of the crustal thickening. The first-order estimates presented on Fig. 1(a) assume wedge symmetry and, therefore, the balance for the retro-wedge is the same.

The relative role of the compressional force decreases as the wedge grows (Medvedev 2002). This is illustrated by the ratio $F_c/F_t \sim (h_{\max}/\lambda_c)^2$, which decreases because λ_c increases more rapidly than $h_{\max}$. Therefore, after some growth the balance between basal traction and gravity ($F_t \sim F_g$) is the main control on the wedge evolution. Resolving this balance for the ratio of the system thickness (Δh) to the horizontal length scale (λ_c) gives the crude estimate of the wedge taper as

$$\Delta h/\lambda_c \sim \eta_c V/\left(\Phi \rho_c g h_a^2\right) \tag{2}$$

Note that Δh and λ_c are the characteristic length scales for F_g and F_t and, therefore, the right side of eq. (2) represents the ratio of average stresses corresponding to these forces. This ratio corresponds to the Ramberg number (Rm, Fig. 1a), the main dimensionless parameter of the force balance in the wedge, and shows, for example, that wedges characterized by lower Rm are generally steeper (see Section 4.1 and Medvedev 2002).

For the second orogenic case (Fig. 1b) the conceptual model includes a hot, low viscosity layer, η_b, in the lower crust. The simplest parametrization assumes a critical depth, z^* (Fig. 1b), as a proxy for the transition from high to low viscosity, but other formulations discussed later more correctly consider a critical temperature, T^*, or a depth or temperature range over which the transition occurs. The forces are estimated in the same manner as those for the first case. To first order we again neglect F_c and the estimate of F_g remains unchanged. Shear stresses from the basal traction, F_t, are necessary to maintain lateral gradients in crustal thickness and counteract the role of gravity, which tends to relax these gradients. The total traction, F_t, comprises two parts, F_{tc} and F_{tb}, which depend on the viscosity of the material in contact with the underlying mantle lithosphere (Fig. 1b).

Three crustal geometries exist, depending primarily on η_b/η_c. First, the uniform viscous geometry, has $\eta_c = \eta_b$ as described above and predicts back-to-back wedges. If η_b decreases somewhat F_{tb} can still support some wedge taper in the central region of the thickened crust, while F_{tc} supports a higher wedge taper at the edges of the deformed crust. This leads to the second geometry, wedges each with dual tapers, an external surface slope that is steeper than the internal one. In the third geometry η_b, and F_{tb}, are too small to support any significant taper or surface slope and the corresponding geometry is a plateau flanked by wedges supported by F_{tc} (Fig. 1b).

In the third geometry the force balance eq. (1) further simplifies to $F_g - F_{tc} \sim 0$. The rheological transition $\eta_c \rightarrow \eta_b$ along the Moho limits the value of F_{tc}; which in turn limits F_g and,

(a) Orogenic crust with uniform rheology (wedge phase):

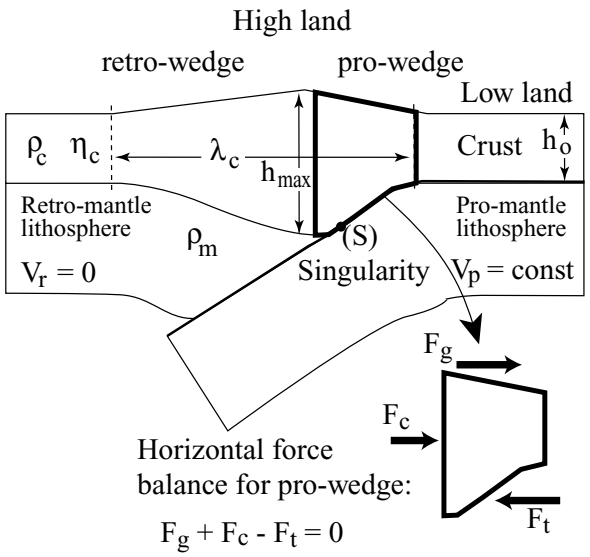

- Gravity force :

$$F_g \sim \rho_c \Phi g \hat{\ell} \frac{h_{max}^2 - h_o^2}{2} = (\rho_c \Phi g \hat{\ell} h_a) \Delta h$$

- Compressive force :

$$F_c \sim \left(\eta_c \frac{V_p}{\lambda_c}\right) \hat{\ell}\, h_{max}$$

- Basal traction force :

$$F_t \sim \left(\eta_c \frac{V_p}{h_a}\right) \hat{\ell} \lambda_c$$

Ramberg number:

$$Rm = \frac{F_g / \Delta h}{F_t / \lambda_c}\bigg|_{t=0} = \frac{\rho_c \Phi g h_o^2}{\eta_c V_p}$$

(b) Orogenic crust with layered rheology (plateau phase):

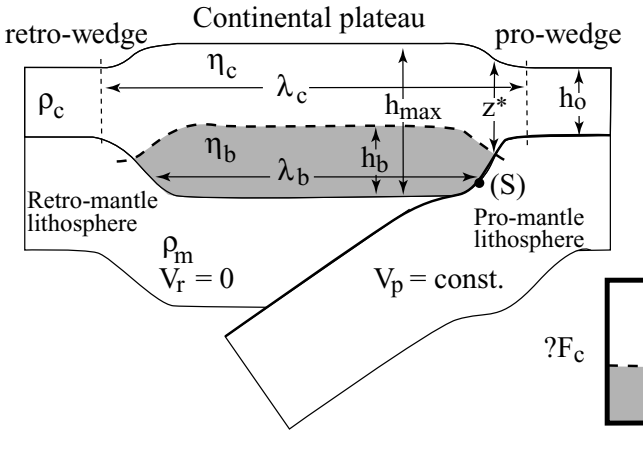

- Basal traction force :

$$F_t = F_{tc} + F_{tb}$$

$$\sim \frac{\eta_c V_c}{(h_o + z^*)/2} (\lambda_c - \lambda_b) \hat{\ell} + \frac{\eta_b V_b}{h_b} \lambda_b \hat{\ell}$$

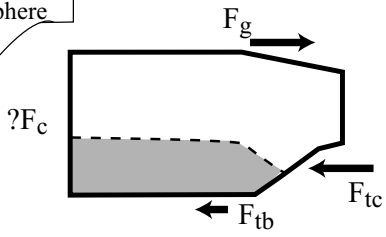

Horizontal force balance for plateau

$$F_g - F_{tc} \approx 0$$

Figure 1. Conceptual illustration of the physical basis of the model for wedge and plateau phases. In the subduction model deformation is driven by convergence of pro-lithosphere at velocity V_p and by detachment and subduction of the pro-mantle lithosphere at point S. Retro-mantle is stationary, $V_r = 0$. The forces derive from gravity, F_g, compression, F_c, and traction acting at the base of the crust, F_t. An estimate of the horizontal force balance is given for the pro-side of the deformed crust. (a) Orogenesis of crust with uniform viscosity (η_c) leads to the formation of back-to-back wedges. The Ramberg number, Rm, the ratio of characteristic gravity and shear stresses of the system, controls the behaviour of the wedge phase of orogenesis. (b) Orogenesis of the crust with layered rheology may lead to formation of a plateau when $\eta_c \gg \eta_b$ and $F_{tb} \to 0$. Basal traction force, F_t, is divided into two parts reflecting the changes at the base of crust due to formation of the weak basal layer, F_c is neglected in simplified force balance, F_g is independent of viscosity and estimated as in (a). ρ_c = density of crust, ρ_m = density of mantle, $\phi = (1 - \rho_c/\rho_m)$ = isostatic amplification factor, $\Delta h = (h_{max} - h_0)$ = maximum crustal thickening, $h_a = (h_{max} + h_0)/2$ = average thickness of the crustal wedge, $\hat{\ell}$ = unit length normal to the model plane. See Tables 1 and 2 for definitions and text for details.

therefore, determines the thickness of the resulting plateau crust. Thus, once a plateau develops ($F_{tb} \ll F_{tc}$), the plateau crustal thickness is insensitive to the properties of the weak basal layer (η_b and h_b) and is determined mainly by the properties of the cold crust and parameters that limit value of F_{tc} (e.g. z^*).

The development of the weak lower crust can be explained by the decrease in effective viscosity with increasing temperature. The associated thermal evolution is controlled by three fundamental processes—self-heating from the decay of long-lived radioactive elements, advection, and conduction (Fig. 2). During convergence a crustal layer, thickness h_r, with uniform radioactive heat production, A, thickens and heats itself (Fig. 2).

Thermal advection is proportional to the product of the velocity and the temperature gradient in the direction of motion. We distinguish both horizontal advection, owing to convergence, and vertical advection, owing to vertical material stretching. Horizontal advection is not important early in the evolution when horizontal temperature gradients are small. Crustal thickening causes material stretching and significant vertical advection of heat (Fig. 2). In addition, the downward component of motion of the subducting slab

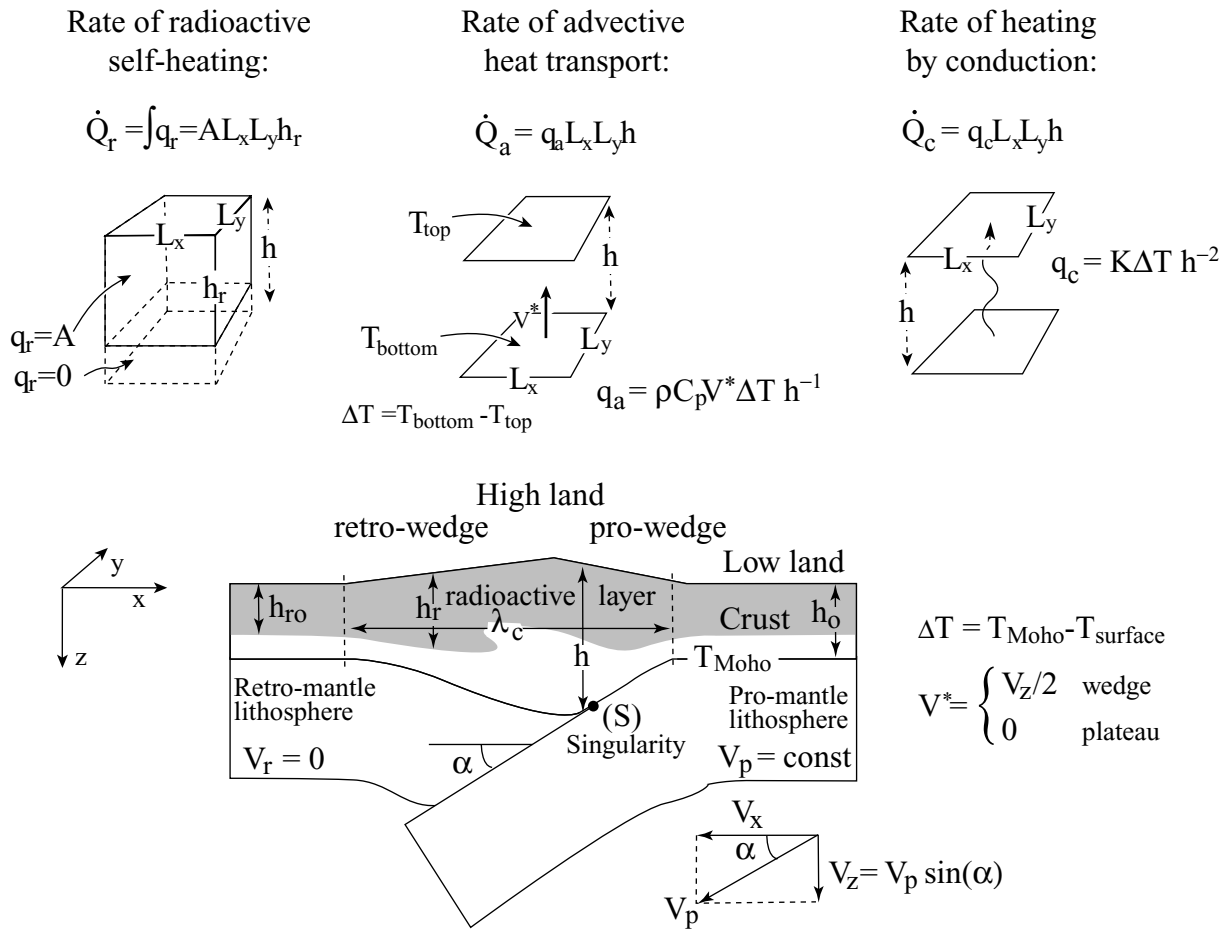

Figure 2. The thermal evolution of the model orogenic crust is controlled by the interplay among crustal heating by radioactive decay, heat advection associated with the displacement of rocks, and conduction of heat that relaxes temperature gradients. Estimates of the corresponding local gradients of heat fluxes (q_r, q_a, q_c) can be integrated to give approximate rates of heating ($\dot{Q}_r$, $\dot{Q}_a$, $\dot{Q}_c$) for a typical vertical crustal column of height h, bounded by the model top surface and the Moho at the bottom, with horizontal length scales L_x and L_y (top panel) and across which temperature varies by ΔT. See text for details. A = volumic rate of heat production of the radioactive crust of thickness h_r, ρ = average density of the system for the thermal model, K =thermal conductivity, V^* =average vertical crustal velocity; V_z = vertical velocity at the top of retro-slab (=V_p sin (α) at $t \sim 0$). Other parameters and values are given in Tables 1 and 2 and Fig. 1.

(velocity V_z, Fig. 2) also advects heat and this effect is strongest on the retro-side of the system, resulting in some cooling of retro-mantle and crust.

The estimate of conduction (Fig. 2) measures the mean rate of heating, or cooling, of a steady state purely conductive layer of the crust when the heat flux into the base of the layer, or out of the top, is instantaneously changed by an amount equal to the steady state flux. That is, the rate of heating is proportional to the difference in the heat flux into and out of the layer. This change creates curvature of the geotherm which results in the heating or cooling. For example, it provides a measure of the mean cooling rate of a steady state conductive crust when rapid advection of cold subducting mantle beneath the crust temporarily reduces the heat flux into the crust significantly. Similarly, the same estimator measures the mean rate of crustal heating when the top of a conductive layer is perfectly blanketed, or is subject to a temperature state that causes a significant decrease of the heat flux out of the conductive layer. The conductive diffusion of heat from the thickened radioactive upper crust is a major mechanism of heating of the lower non-radioactive crust during deformation.

Using the first-order scaling analysis (Fig. 2) and the parameter values (Table 1), we estimate that in the models considered here, all three thermal components are significant, especially during the initial stages of deformation, and therefore none of them can be neglected. The thermal control differs significantly between the wedge and plateau phases. During crustal thickening the vertical material advection, which at a given depth replaces hotter material with cooler material, competes with self-heating and conduction from the mantle and upper crust. Vertical advection is, however, negligible in the plateau crust because the thickness remains almost constant ($V_z \sim 0$). Horizontal motion correspondingly increases during the plateau phase and the radioactively thickened crust is transported backwards, thereby increasing the role of horizontal advection. Owing to the combined effects of horizontal advection, conduction, and self-heating, the hottest crust is located below the retro-plateau.

3 THE THERMAL–MECHANICAL MODEL

A fully thermally coupled, plane strain, incompressible viscous-plastic model (Fig. 3) is used to investigate deformation of a model domain subject to velocity boundary conditions that correspond to subduction of the underlying mantle lithosphere. The mechanical problem is restricted to the calculation of the deformation of the

Table 1. Definition of model parameters.

Variable	Definition	Standard value [Initial value]
h	Crustal thickness (Figs 1 and 2)	$[h_o = 35$ km$]$
h_b	Thickness of low-viscosity layer (Fig. 1b)	$[h_{bo} = 0$ km$]$
Δh	Maximum crustal thickening (Fig. 1)	$\Delta h = \max(h - h_o)$
w	Elevation of topography (Fig. A)	$[w_o = 0$ km$]$
z	Depth below surface	–
λ_c	Width of deformed area (Fig. 1)	–
λ_b	Width of low-viscosity layer (Fig. 1b)	–
g	Acceleration due to gravity	9.81 m s^{-2}
t	Time	0–75 Myr
Δx	Convergence (in km)	$\Delta x = V_p \cdot t$
ρ_c	Density of crust	2700 kg m^{-3}
ρ_m	Density of mantle	3300 kg m^{-3}
Φ	Isostatic amplification factor (Fig. 1)	0.18
η_c	Viscosity of crust (Fig. 1)	10^{23} Pa s
η_b	Viscosity of basal layer in crust (Fig. 1b)	–
z^*, z_1/z_2	Depth (effective depth) of rheological transition (Figs 1b, 3 and 17f)	40 km, 40/50 km
ϕ	Internal angle of friction	7.5°
c_o	Cohesion	10^6 Pa
V_p	Convergence velocity, pro-side (Figs 1 and 2)	1 cm yr^{-1}
D	Flexural rigidity	10^{22} N m
T	Temperature	–
T_{top}	Temperature at the top surface	0°C
T_{Moho}	Temperature at the Moho (Figs 2, 3 and 17c)	$[T_{\text{Moho}} = 644$°C$]$
ΔT	Difference in temperature between Moho and upper surface (Fig. 2)	$[\Delta T_{\text{o}} = 644$°C$]$
T^*, T_1/T_2	Temperature(s) of rheological transition (Fig. 3)	700°C, 400/700°C
C_p	Heat capacity (Fig. 2)	750 J (kg K)$^{-1}$
ρ	Average density of the system (used in thermal model; Figs 2 and 3)	3000 kg m^{-3}
K	Thermal conductivity (Fig. 2)	2.25 W (m K)$^{-1}$
κ	Thermal diffusivity (Fig. 2)	10^{-6} m^2/s
q_s	Surface heat flux (Fig. 3)	$[q_{so} = 70$ W m$^{-2}]$
q_m	Mantle heat flux (Fig. 3)	30 W m^{-2}
h_r	Thickness of radioactive layer (Figs 2 and 3)	$[h_{ro} = 20$ km$]$
A_1	Volumic rate of heat production in radioactive layer (Figs 2 and 3)	2×10^{-6} W m^{-3}
A_2	Volumic rate of heat production in the lower crust (Figs 3 and 16)	0 μW m^{-3}
Kp	Plateau coefficient (Appendix A)	–
E	Effective width of thickening (Appendix A)	–

model crust with basal boundary velocity equal to V_p beneath the convergent (pro-) crust and decreasing to $V_p = 0$ beneath the stationary (retro-) crust. The velocity transition occurs at S, where the pro-mantle detaches and subducts (Fig. 3a). The domain of the thermal model includes the crust and underlying lithosphere. This is necessary because the assumed subduction influences the temperature in the overlying crust. A kinematic velocity field corresponding to the mantle subduction (Fig. 3b) is used in the solution of the advective-diffusive thermal problem in the subcrustal lithosphere, whereas the dynamic velocity field from the solution of the mechanical problem is used in thermal solution in the crust. The results presented focus on the fully dynamic thermal–mechanical part of the solution for the crust.

The crust has an upper free surface and most models include flexural isostatic compensation of the thickened crust calculated from the elastic flexure of a continuous uniform beam, flexural rigidity, D (Table 1), embedded in the model at the base of the crust. For the models discussed here the results are not significantly different from those where a beam broken at S is used (Jamieson *et al.* 2002). A range of crustal rheologies is considered, including frictional plasticity, uniform linear viscosity, depth-dependent linear viscosity, and temperature-dependent viscosity, as defined in Fig. 3.

The boundary conditions for the thermal model are constant temperature at the surface (0°C), constant basal heat flux, $q_m = 30$ mW m^{-2} (applied to the bottom boundary of the subducting slab), and no heat flux along the lateral boundaries. The initial temperature field is calculated assuming a steady state for the initial geometry and $V_p = 0$. The results do not depend strongly on whether the initial conditions assume no precursor subduction or prolonged subduction with $V_p = 1$ cm y^{-1} (Vanderhaeghe *et al.* 1998). We therefore restrict the models considered here to those with an initial conductive equilibrium, which for the standard model parameters yields a Moho temperature of 644 °C. The thermal model properties include uniform radioactive heat production A_1 in the upper crust and, in a few models, heat production A_2 in the lower crust (Section 5.2). Other standard model parameter values are given in Table 1.

The model evolution is calculated using an arbitrary Lagrangian–Eulerian (ALE) method for the finite element solution of thermal and incompressible viscous-plastic creeping flows (Fullsack 1995). Thermal and mechanical calculations are based on the equations (Fig. 3) and are alternated so that mechanical properties can be updated according to the current temperature field. An advection/interpolation algorithm allows the associated Lagrangian motion to be followed and the field properties transferred to the

Thermal formulation: $\rho C_p \partial T/\partial t = \underset{\text{production}}{A} + \underset{\text{diffusion}}{K \nabla^2 T} - \underset{\text{advection}}{\rho C_p V \cdot \nabla T}$

Mechanical formulation

Momentum balance: $\nabla \cdot \sigma_d - \nabla P + \rho g = 0$

Incompressibility: $\nabla \cdot v = 0$

Rheology

Frictional plastic: $J_2(\sigma_d) \leq P \cdot \sin\phi + c_o$

or

Viscous creep: $\sigma_d = 2\eta\dot{\varepsilon}$

Viscosity profile as a function of depth (z) or temperature (replace z by T):

Step-function model [$V(\gamma_c/\gamma_b)z(z^*)$]:

for $z \leqslant z^*$: $\eta = \eta_c = 10^{\gamma_c}$ Pa s

for $z > z^*$: $\eta = \eta_b = 10^{\gamma_b}$ Pa s

Linear decrease model [$V(\gamma_c/\gamma_b)z(z_1/z_2)$]:

for $z \leqslant z_1$: $\eta = \eta_c = 10^{\gamma_c}$ Pa s

for $z_1 < z \leqslant z_2$: $\eta = \eta_c + (\eta_b - \eta_c)\dfrac{(z_1 - z)}{(z_1 - z_2)}$

for $z > z_2$: $\eta = \eta_b = 10^{\gamma_b}$ Pa s

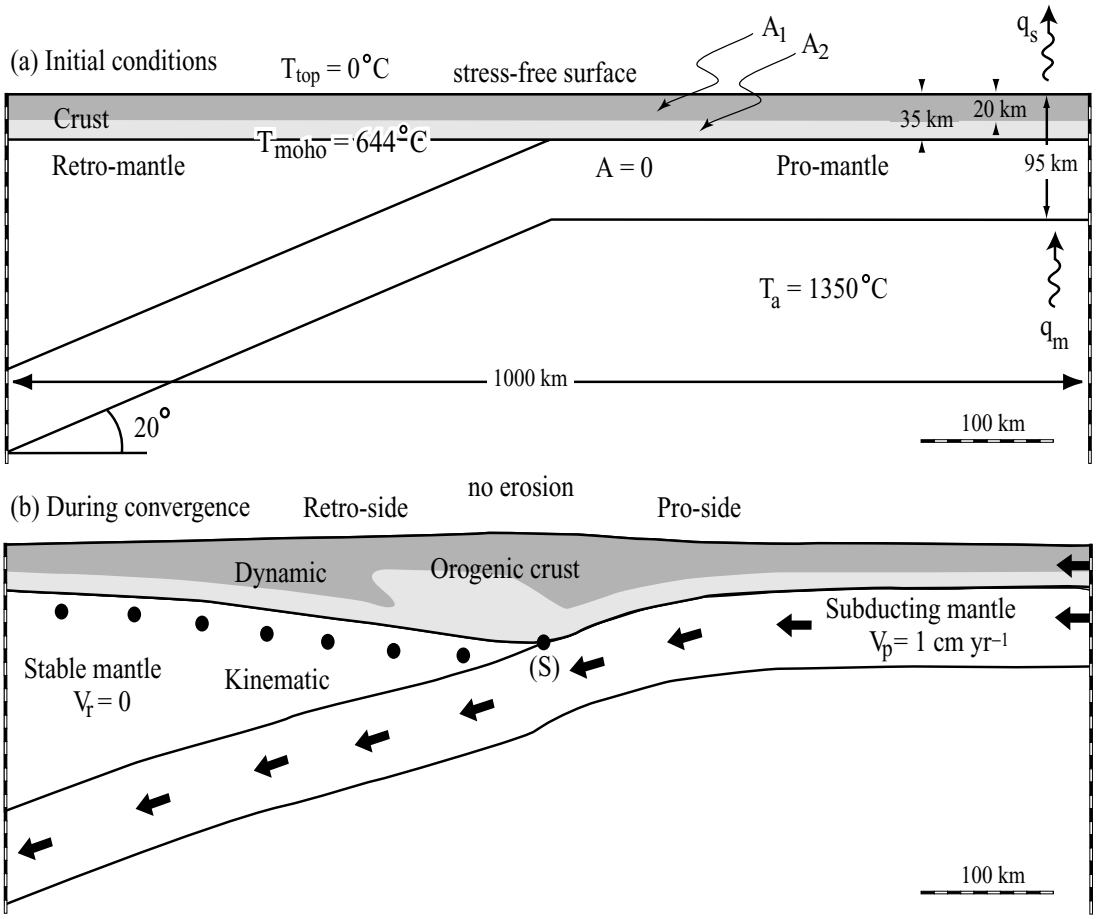

Figure 3. Thermomechanics, rheology, geometry, and boundary conditions of the numerical model. Diagrams depict (a) initial geometry and (b) deformed geometry. Mechanical deformation is considered for the crust only, which subjected to kinematic boundary conditions at the Moho and a stress-free upper surface. Below the crust the model is kinematic, with convergence of pro-mantle lithosphere at constant velocity V_p (arrows), detachment at S, and subduction beneath stationary retro-mantle ($V_r = 0$; dots). The subducting slab is modelled kinematically and is deflected vertically by an amount equal to the thickness of the isostatic crustal root. Thermal model includes crust, and pro- and retro- mantle. Thermal boundary conditions: no heat flux through lateral boundaries; surface temperature $T = 0°C$; and constant heat flux at the bottom, $q_m = 30$ mW m^{-2}. Temperature in the lithosphere is limited by $T_a = 1350°C$ (thermal diffusivity of asthenosphere is very large to simulate thermal effect of convection). Initial temperature profile in the model is calculated for conductive steady state. Heat-producing layer (dark grey) has $A_1 = 2\ \mu$W m^{-3} and is initially 20 km thick. Various rheologies and styles of isostasy considered are described in Table 2. In the mechanical formulation, σ_d = deviatoric stress; $J_2(\sigma_d)$ =second invariant of deviatoric stress tensor; P = confining pressure; ε = strain rate. Other parameters, units, and values as defined in Table 1 and Figs 1 and 2.

evolving Eulerian finite element grid. The results presented below use an Eulerian grid with 200 × 27 elements for the crustal mechanical calculations, and 200 × 40 elements for the lithospheric scale thermal calculations. The crustal Lagrangian grid has 500 × 27 elements.

Two types of models are investigated. In the first type (Sections 4, and 5.1), both the mechanical and thermal evolution are calculated and the dynamic (crustal) and kinematic (subcrustal) velocities are used in the thermal advection. There is, however, no feedback coupling of thermal properties to the mechanics because the model properties (plasticity, viscosity, density) are either constant or do not depend on temperature. In the second type (Sections 5.2 and 5.3), the mechanical evolution is coupled to thermal evolution, but only through the temperature dependence of viscosity. In both types the thermal calculation is made for the entire model domain and the advection velocities are either specified kinematically (subcrustal region) or determined dynamically (crustal region). The shape of the model domain changes with time, but the boundary conditions are constant.

4 MODELS WITH CONSTANT RHEOLOGICAL PROPERTIES

In order to investigate the rheological control on model dynamics, we first describe results from models with uniform viscous and frictional–plastic rheologies that do not change as the model evolves. By first comparing models with no isostatic compensation (Section 4.1), we focus on the fundamental differences in rheological controls. The role of isostatic compensation (flexural or local isostasy) is then assessed (Section 4.2) based on models with similar uniform viscous and frictional–plastic rheologies. The impact of deformation style on thermal evolution is discussed in Section 4.3, using models with simple rheologies in order to facilitate comparison with the more complex rheological models discussed later. A more detailed analysis of viscous wedges is developed elsewhere (Medvedev 2002).

4.1 Mechanical evolution of a single-layer crust

The main features of these models can be described by comparing a frictional–plastic model ($\phi = 11.3^\circ$) with uniform constant viscosity models that are roughly similar in their geometrical evolution (Fig. 4). Other parameter values are given in Table 1 and the models are described in Table 2. In these models convergence is accommodated by the progressive development of back-to-back wedges. Pro-side velocities reflect rigid transfer of material, and near-surface velocities decrease in the vicinity of the singularity. The vertical velocity profile is inverted across the singularity with a transfer of the maximum velocity from the base to the surface. The singularity in the basal velocity at *S* imposes a localised thickening across the

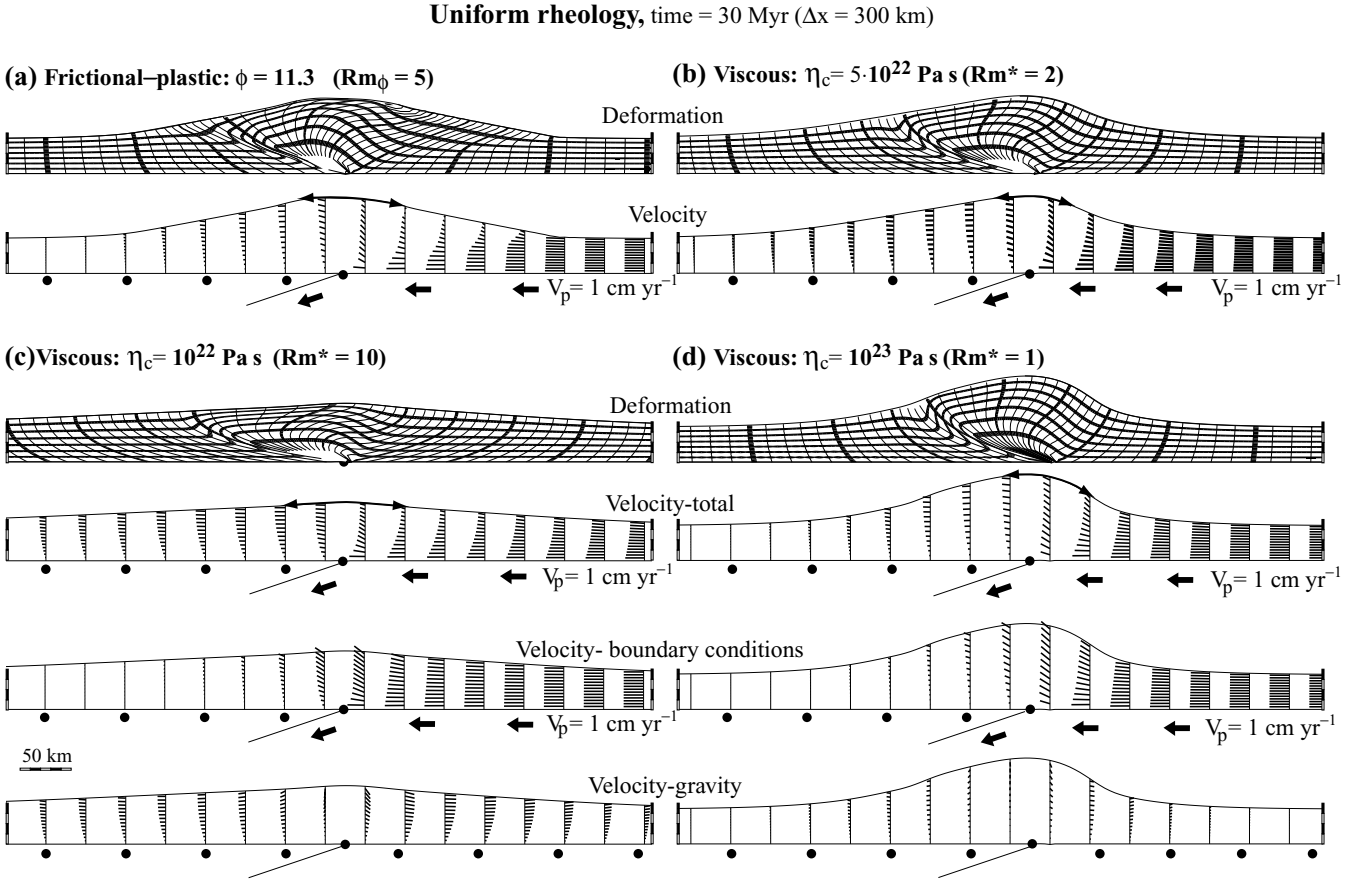

Figure 4. Comparison of frictional–plastic (a) and uniform constant viscous (b, c, d), model results at $t = 30$ Myr. Models have various Rm and Rm_ϕ values (see Fig. 1 and text) and no isostatic compensation. Upper panels of (a–d) show deformation of a coarse Lagrangian grid; lines are passively advected markers. Lower panels of (a) and (b) show velocity distribution within the crust (short lines), basal boundary velocity (heavy arrows and dots), and region of instantaneous extensional strain at the model surface (lines with two arrowheads). For (c) and (d), the lower panels show the total velocity field, and decomposition of this field into components that are driven by the boundary conditions ($g = 0$) and by gravity ($V_p = 0$).

Table 2. Description of models.

Models	Comments, description	Parameters variations
	Uniform rheology models (Figs 4, 5, 7 and 8)	
$FP(\xi)$	Frictional plastic rheology with internal friction $\phi = \xi^\circ$	$\xi = 7.5$–15
$V(\xi)$	Uniform crust with viscosity $\eta = 10^{\xi}$ Pa s	$\xi = 22$–23
	Isostatic compensation (Fig. 6):	
noIso	Prevent any vertical motion along the base of crust	ρ_m is very high
Airy	Local isostasy	D is very low
	Depth-dependent rheology of crust (Figs 3, 9–12):	
$V(\gamma_c/\gamma_b)z(z^*)$	Viscosity decreases from $\eta_c = 10^{\gamma c}$ Pa s to $\eta_b = 10^{\gamma b}$ Pa s at depth $z = z^*$ km	$\gamma_c = 23$; $\gamma_b = 18$–22; $z^* = 40$–50
$V(\gamma_c/\gamma_b)z(z_1/z_2)$	Viscosity linearly decreases from $\eta_c = 10^{\gamma c}$ Pa s to $\eta_b = 10^{\gamma b}$ Pa s at in the interval of depth $z = [z_1, z_2]$ km	$\gamma_c = 23$; $\gamma_b = 18$–22; $z_1 = 40$; $z_2 = 50$
	Temperature-dependent rheology of crust (Figs 3, 13–17):	
$V(\gamma_c/\gamma_b)T(T^*)$	Viscosity decreases from $\eta_c 10 = ^{\gamma c}$ Pa s to $\eta_b = 10^{\gamma b}$ Pa s at temperature $T = T^*$ $\{\}^\circ$C	$\gamma_c = 23$; $\gamma_b = 18$–22; $T^* = 700$
$V(\gamma_c/\gamma_b)T(T_1/T_2)$	Viscosity linearly decreases from $\eta_c = 10^{\gamma c}$ Pa s to $\eta_b = 10^{\gamma b}$ Pa s at in the interval of temperature $T = [T_1, T_2]^\circ C$	$\gamma_c = 23$; $\gamma_b = 18$–22; $T_1 = 400$; $T_2 = 700$

detachment point marked by the activation of conjugate shear-zones rooting at the singularity. The uplifted region has a triangular geometry throughout the model evolution expressed by a constant plateau coefficient (Appendix A), $K_p \sim 0.5$.

A decrease in the near-surface horizontal velocities from the pro-side to the retro-side in the vicinity of S indicates instantaneous horizontal extension in this region (Figs 4a and b). This is not observed at the onset of thickening and only appears during the evolution of the model. Finite deformation of the crustal layer, as delineated by the Lagrangian marker grid, is characterized by the development of a broad antiform overthrust along the retro-side shear zone.

The main differences between the uniform viscous and frictional plastic models are in the symmetry of the back-to back wedges and in the style of internal deformation. Back-to-back wedges formed during the evolution of the frictional plastic model do not show any visible asymmetry from 0 to 75 Myr (Fig. 4a). In contrast, the viscous model is asymmetric with steeper slopes on the pro-side (Figs 4b–d). The more diffuse character of deformation in the viscous model compared to the frictional–plastic one is evident from broader shear zones emanating from *S*. In the frictional–plastic model, the orogen grows by foreland propagation of the conjugate shear zones, whereas in the viscous model growth is accompanied by diffuse deformation ahead of the shear zones.

Comparison of wedges with differing viscosities illustrates the influence of strength; the higher the viscosity, the higher and narrower the wedge for a given amount of convergence (Figs 4b–d). This behaviour is explained by the effect of gravitational relaxation on a viscous wedge. The lower panels in Figs 4(c) and (d) show the relative contributions of boundary conditions (flow calculated with $g = 0$) and gravitational forces (flow calculated with $V_p = 0$) to the total velocity field. The velocity field from the boundary conditions is similar in both cases, but the velocity due to gravity, which causes material to flow down thickness gradients, is larger for low viscosities (high Rm), which explains the reduced thickness of the corresponding wedges and supports the predictions of Section 2 (eq. 2).

Owing to the simple approximately triangular geometry, the evolution of the models can be described by the maximum crustal thickness, $h_{\max}(t)$, at a given time, and the averaged surface slope of the two back-to-back wedges (Fig. 5). The maximum thickness increases without limit; however, the rate of increase of $h_{\max}(t)$ decreases with time (Fig. 5a) because a constant mass flux into the wedges results in slower growth as the wedges become larger. The rate of growth depends on the rheology, with high η and high ϕ wedges resulting in greater thickness. Model geometries for viscous layers reflect their Rm ratios (Fig. 1), which range from Rm = 1 ($\eta_c = 10^{23}$ Pa s) to Rm = 10 ($\eta_c = 10^{22}$ Pa s) (Figs 4 and 5), and maximum thickness is inversely dependent on Rm.

Following Willett (1999), we introduce Rm_ϕ, the frictional–plastic analogue of Rm. When critical, frictional–plastic tangential and normal stresses are related by $\tau = \sigma_n \tan \phi$. When normal stress is approximately equal to the lithostatic pressure, $\mathrm{Rm}_\phi = 1/\tan \phi$, by analogy with the viscous case (Fig. 1). The viscous and frictional–plastic Ramberg ratios as defined here are not exactly equivalent because Rm is the result of an approximate force balance calculation, whereas Rm_ϕ expresses critical behaviour of frictional–plastic wedges. For example, a frictional–plastic model with $\mathrm{Rm}_\phi = 5$ ($\phi = 11.3^\circ$) has a closer correspondence to a viscous model with Rm = 2 ($\eta_c = 5 \times 10^{22}$ Pa s) than to one with Rm = 5 ($\eta_c = 2 \times 10^{22}$ Pa s) (Fig. 5).

The difference between frictional–plastic and viscous rheologies is more obvious when average slopes are compared (Fig. 5b). The averaged mean slope is simply the ratio of maximum elevation to half the horizontal length scale for each of the back-to-back wedges. Initially, all models show increasing average slope as they grow from an initially horizontal layer to a mature wedge. Plastic wedges evolve in a self-similar manner with constant slope. In contrast, viscous wedges evolve through three phases (Fig. 5b): the initial phase occurs by vertical growth (increasing mean slope), the second phase displays close to self-similar growth (approximately constant mean slope), and the third phase involves horizontal spreading that is faster than vertical growth (mean slope decreases). This qualitative difference can be explained using the force balance approach introduced in Section 2. Similarly to the viscous case, the three major forces (gravity, compressive, and basal traction) control the evolution of the frictional–plastic wedges, but they all grow proportionally (Dahlen 1984) resulting in self-similar evolution of the wedge shape. The disproportionate relation between forces for the viscous model (Fig. 1) results in several phases of wedge evolution. The main source of the changes is in the decreasing role of compressive force, F_c, which is still important during the first two phases (Medvedev 2002). The average slope decreases during the third phase in accordance to eq. (2), which is derived ignoring F_c.

Uniform rheology

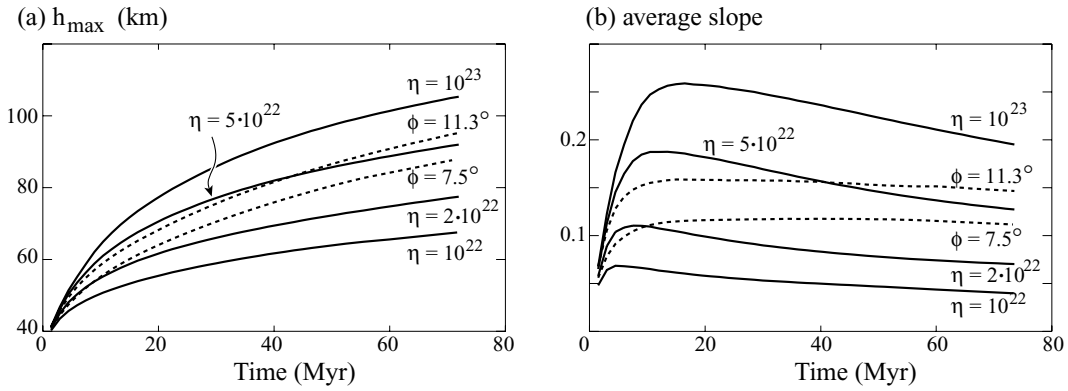

Figure 5. Evolution of maximum crustal thickness, $h_{max}(t)$, and average surface slope, for uniform constant viscous ($10^{22} \leq \eta_c \leq 10^{23}$ Pa s) and frictional–plastic ($\phi = 11.3^\circ$ and $\phi = 7.5^\circ$) models with no isostatic compensation. Some models correspond to those shown in Fig. 4.

4.2 Effect of isostatic compensation model

The effect of Airy and flexural ($D = 10^{22}$ N m) isostatic compensation on uniform viscous (Rm = 1, $\eta_c = 10^{23}$ Pa s) and frictional–plastic ($\mathrm{Rm}_\phi = 7.6$; $\phi = 7.5^\circ$) models is compared with the equivalent uncompensated models after 450 km of convergence at $V_p = 1$ cm y^{-1} (Fig. 6). Isostatic compensation is associated with the development of a thick crustal root and a corresponding decrease in the overall width of the deformed crust. Viscous wedges are asymmetric with maximum crustal thickness on the retro-side.

In the flexural isostasy model (Fig. 6b), part of the weight of the thickened zone is supported by flexural stresses and compensation is achieved over a larger width than in the case of local Airy isostasy (Fig. 6c). Consequently, flexural isostatic compensation results in higher maximum elevations, depressions on the edges of the thickened crust, and a more symmetric root.

The similarity of the flexural and Airy compensation models depends on the relationship between the length scale of deformed crust, λ_c, and the flexural parameter, $\lambda_f = 2\pi(D/\rho_m g)^{1/4}$. When $\lambda_c = 1.8\lambda_f$ the difference between flexural and Airy compensation does not exceed 5 per cent of topography; this is achieved at $\lambda_c \sim 260$ km for $\rho_m = 3300$ kg m^{-3} and $D = 10^{22}$ N m. To a first order, model geometry and velocity fields are not sensitive to the choice of isostatic compensation model ($D \leq 10^{22}$ N m), provided compensation is included, once the length-scale of crustal deformation exceeds about 260 km (Figs 6b and c). In the following models flexural isostatic compensation is used with $= 10^{22}$ N m. This relatively low value was chosen because it is unlikely that high flexural rigidities occur beneath orogenically thickened crust.

4.3 Thermal and mechanical evolution

The thermal and mechanical evolution of frictional–plastic ($\phi = 7.5^\circ$) and uniform viscous ($\eta_c = 10^{23}$ Pa s) models over 75 Myr is shown in Figs 7 and 8. In these models, convergence is accommodated by the continuous growth of back-to-back wedges ($K_p = 0.5$), which share the same general features as those described in 4.1, except for the flexural crustal root.

The thermal evolution of both models is initially dominated by the effect of subduction and crustal thickening; the associated vertical advection causes vertical stretching of the temperature field in the core of the model orogens (Figs 7a and 8a). This effect is opposed by an increase in temperature for each material point owing to increased self-heating as the radioactive layer thickens, which is evident by 45 Myr (Figs 7b and 8b). Heterogeneous thickening of the radioactive layer in the frictional–plastic model (Fig. 7) leads to lateral variations in the efficiency of self-heating and in the distribution of isotherms, whereas a more homogeneous style of thickening in the viscous model (Fig. 8) leads to more uniform heating. Isotherms are inverted toward the edges of the model orogen where vertical advection of heat is more efficient than radioactive self-heating and diffusion.

In both models, crustal isotherms at 75 Myr reflect the geometry of the deformed radioactive layer in the core of orogen. The keel of radioactive material along the retro-step-up shear zone leads to high temperatures and inverted isotherms beneath the retro-wedge. Horizontal and vertical thermal gradients are similar within the deep interiors of each of the wedges (Figs 7c and 8c). Preferential thickening of the upper crustal layer on the pro-side of the *S*-point in the frictional–plastic case leads to maximum temperatures on the pro-side of the system (Fig. 7c), whereas the more homogeneous thickening of this layer in the uniform viscous model produces a generally more symmetrical distribution of crustal isotherms and maximum temperatures that coincide with the radioactive keel beneath the retro-wedge (Fig. 8c). In both cases, lower crustal isotherms are inverted beneath the thermal maximum and isotherms cross the Moho at a high angle beneath the retro-wedge.

5 MODELS WITH DEPTH- AND TEMPERATURE-DEPENDENT VISCOSITIES

Lower crustal weakening is the mechanism proposed in Section 2 for the transition between orogenic phases. Models with simple depth- and temperature-dependent viscosities (Fig. 3) were chosen to illustrate the effect of thermal weakening of the crust, and to compare the results with those where depth is used as a proxy for temperature (e.g. Royden 1996; Shen *et al.* 2001). Models in which there is a step change in viscosity at a critical depth, z^*, or temperature, T^* (Table 2), are the numerical equivalents of the conceptual scale models (Section 2) and may be compared directly. Models in which viscosity decreases over a range of depth or temperature (Table 2) are physically more reasonable and it is important to determine whether these differ significantly from the step-change models.

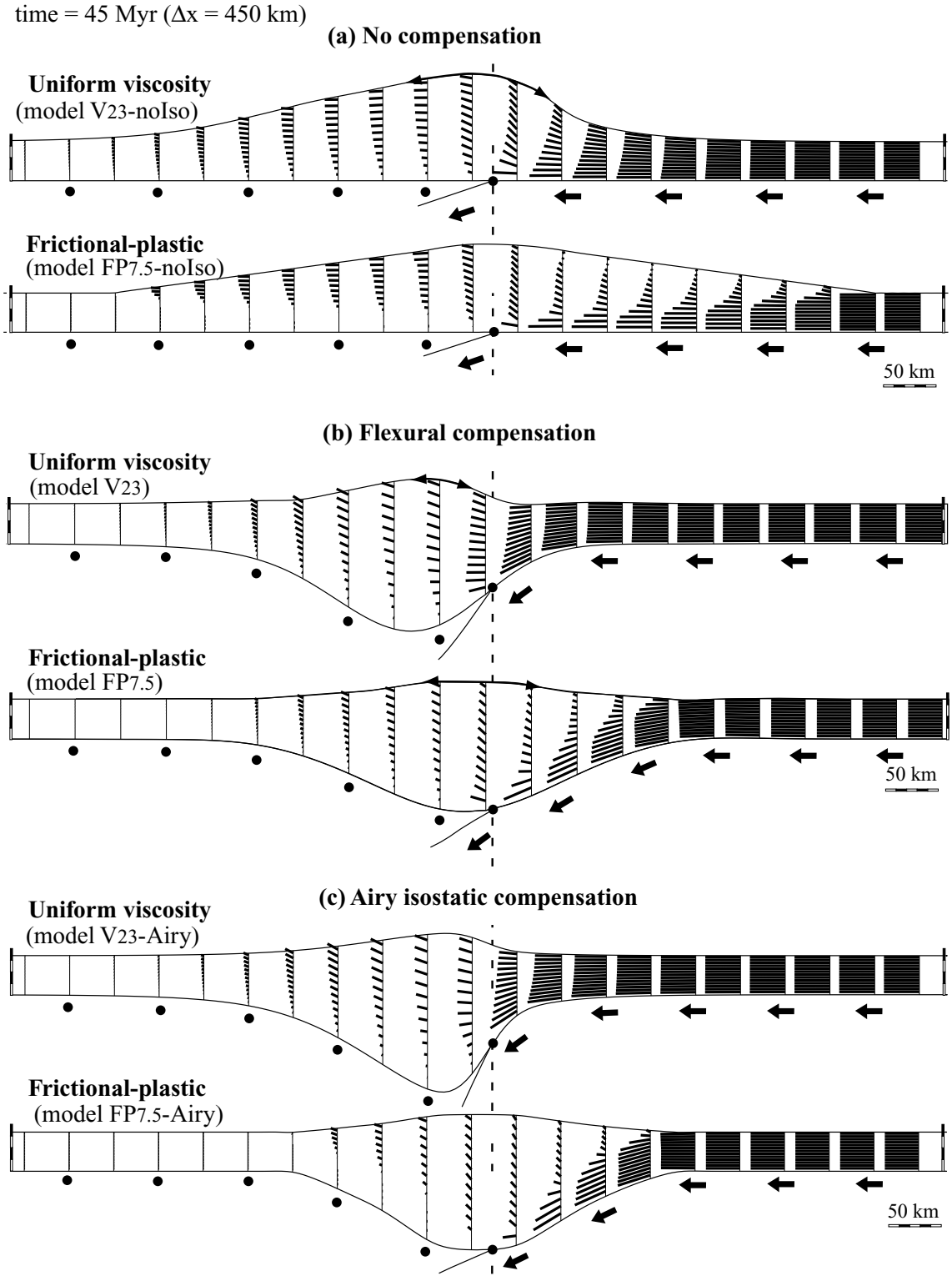

Figure 6. Effect of different styles of isostatic compensation on growth of plastic and viscous wedges. Each pair of diagrams shows the geometry of the deformed crustal layer and velocity field for the models with a constant viscosity, $\eta_c = 10^{23}$ Pa s, (top) and frictional plastic rheology, $\phi = 7.5^{\circ}$, (bottom) after 45 Myr of convergence at a constant rate, $V_p = 1$ cm yr^{-1}. (a) No isostatic compensation. (b) Flexural isostatic compensation calculated for a beam rigidity, $D = 10^{22}$ N m. (c) Airy (local) isostatic compensation. The models are aligned with respect to S.

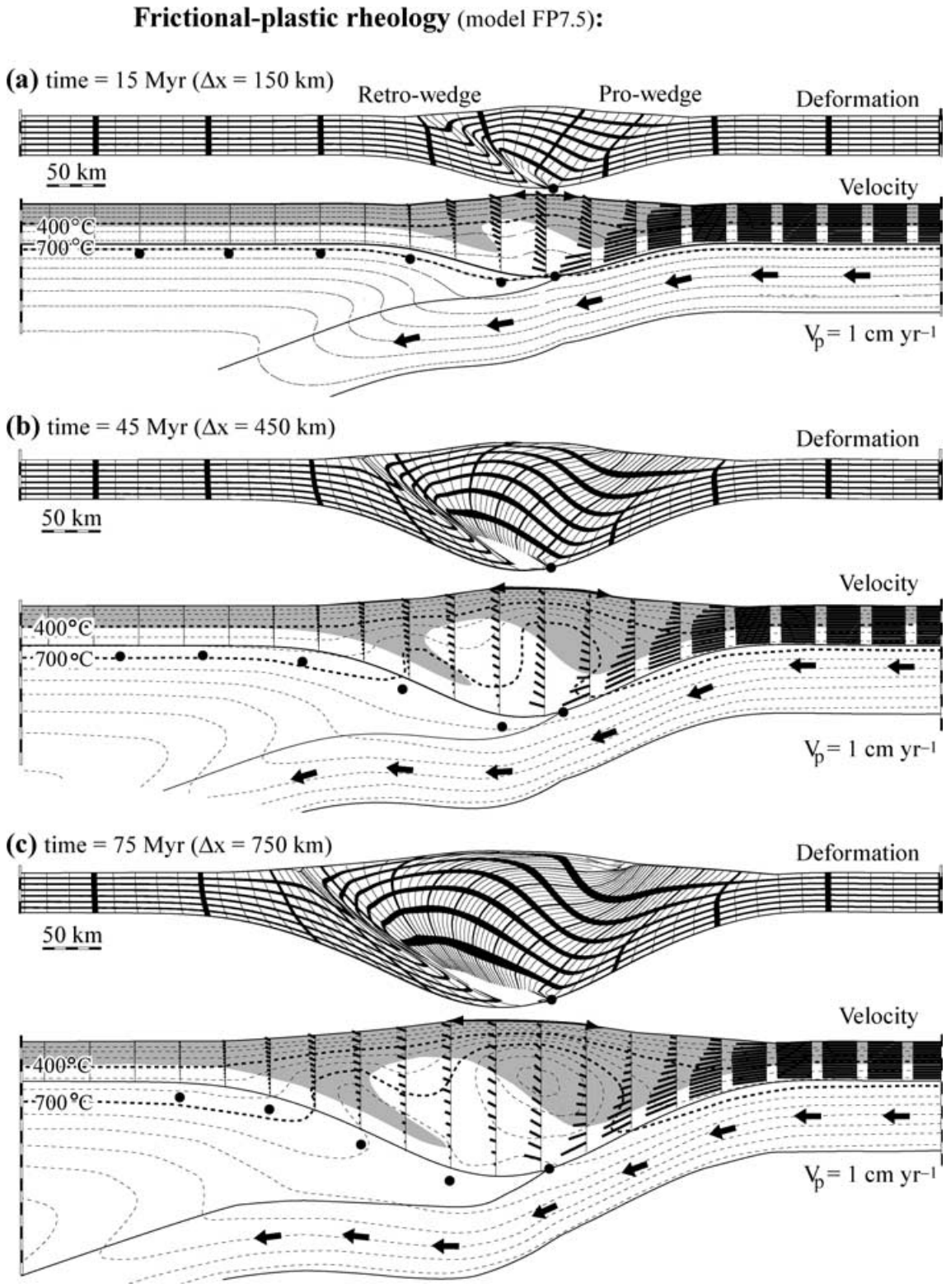

Figure 7. Thermal and mechanical evolution of a model orogen with a frictional–plastic rheology ($\phi = 7.5°$) and flexural isostatic compensation ($D = 10^{22}$ N m). Results are shown after (a) 15 Myr, (b) 45 Myr, and (c) 75 Myr of convergence at a constant velocity, V_p. Upper panel of each pair shows deformation of a coarse Lagrangian grid. Lower panel of each pair shows velocity distribution within the crust (short lines), basal boundary velocity (heavy arrows and dots), and region of instantaneous extensional strain at the model surface (lines with two arrowheads). Isotherms are shown at 100°C intervals (dashed lines). Bold dashed lines delineate the 400°C and 700°C isotherms.

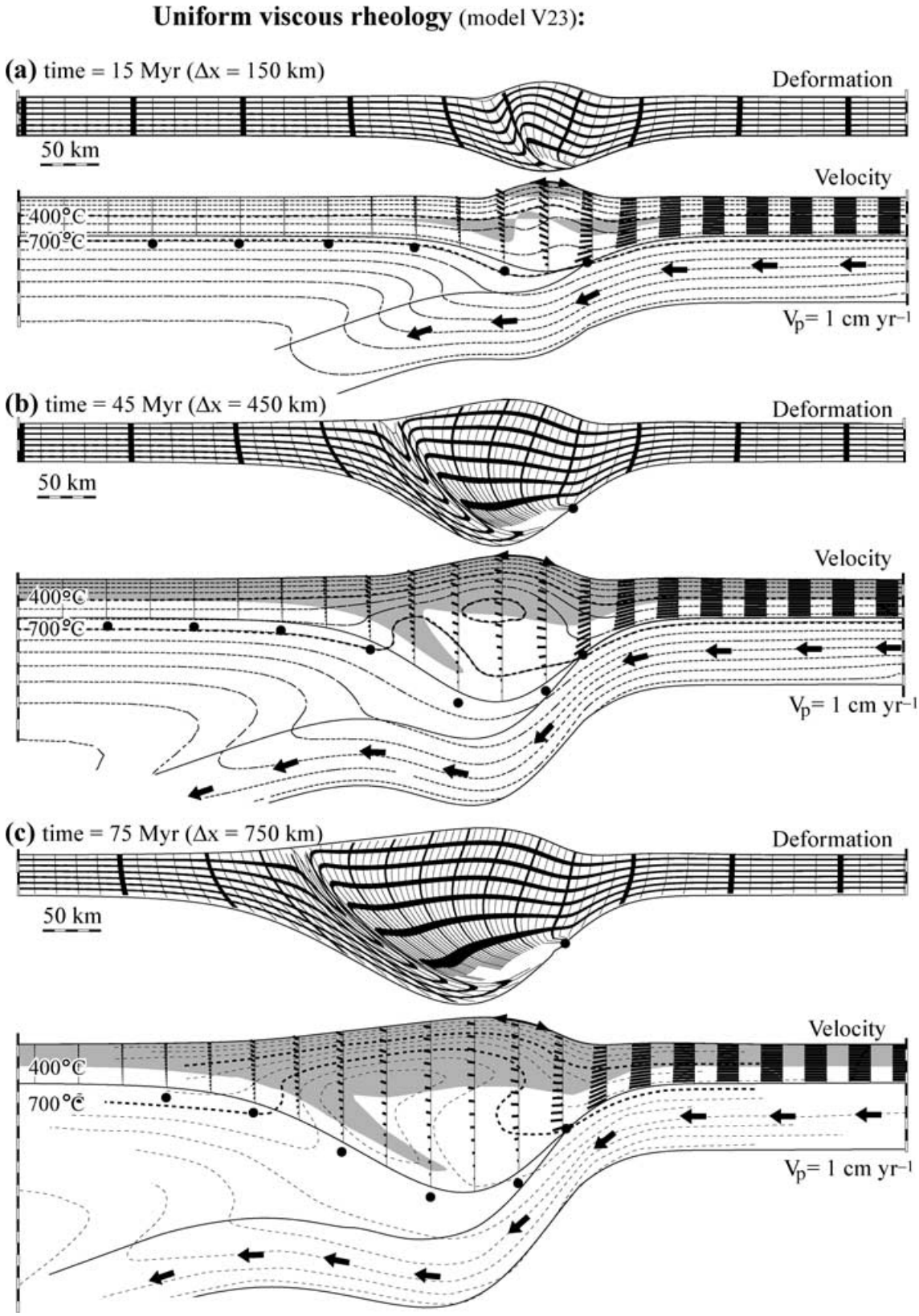

Figure 8. Thermal and mechanical evolution of a model orogen with a uniform constant viscous rheology ($\eta = 10^{23}$ Pa s). Results are shown after (a) 15 Myr, (b) 45 Myr, and (c) 75 Myr of convergence at constant $V_p = 1$ cm yr^{-1}. Other information as in Fig. 7.

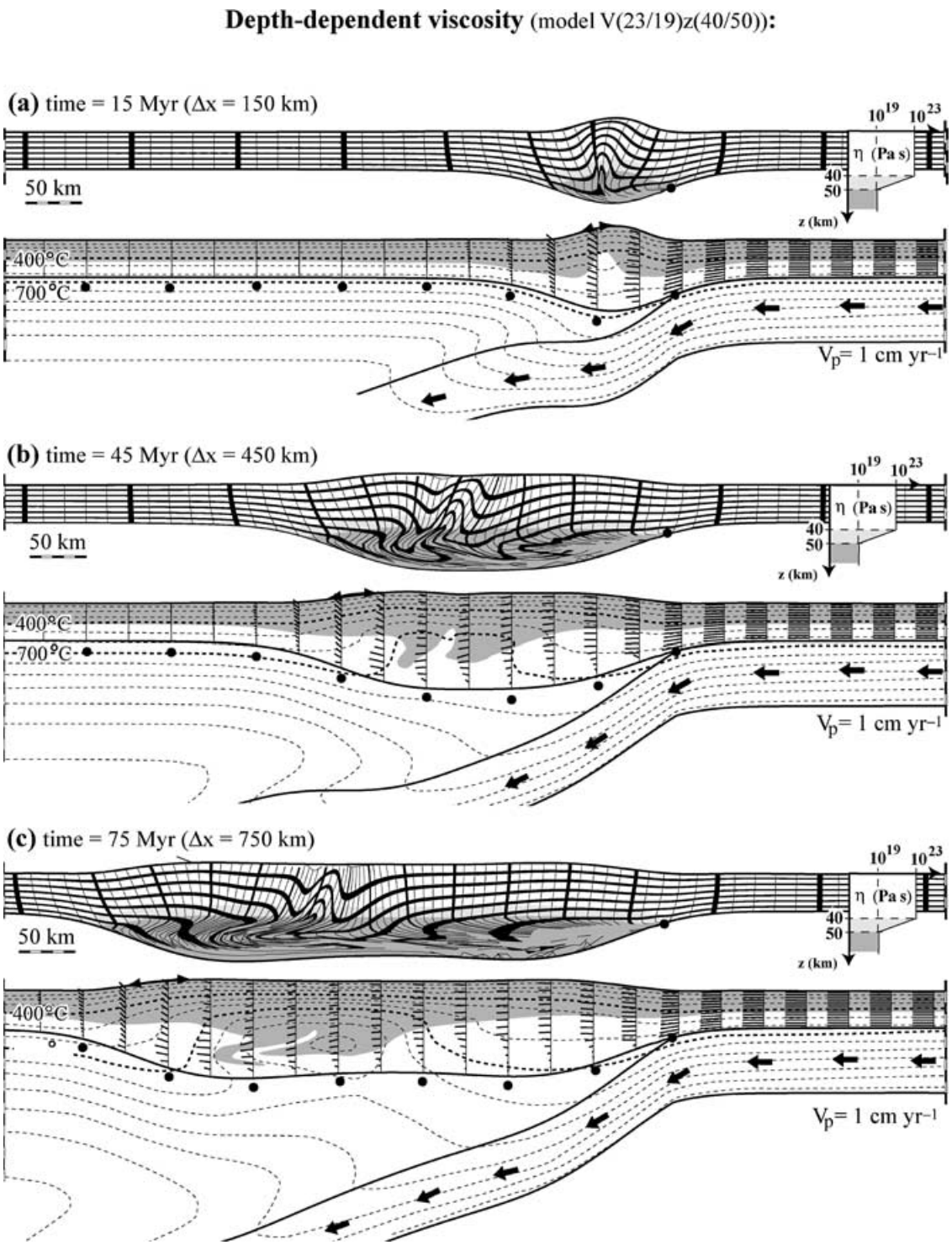

Figure 9. Thermal and mechanical evolution of model V(23/19)z(40/50) with depth-dependent viscosity. The viscosity of the crustal layer in this experiment decreases linearly with depth from 10^{23} Pa s to 10^{19} Pa s between 40 km and 50 km. Results are shown for t = 15 Myr (a), 45 Myr (b) and 75 Myr (c). Upper panel for each pair shows the evolution of the Lagrangian grid and rheology in the crust. Lines are passively advected markers and grey shades represent transition and low viscosity regions (schematic at right). The lower panel in each pair shows velocity distribution in the crust (short solid lines), temperature distribution (dashed lines), and evolution of the radiogenic layer (grey area). See Fig. 7 caption for additional information.

5.1 Depth-dependent viscosity

The evolution of a typical model in which viscosity decreases linearly from 10^{23} Pa s to 10^{19} Pa s between 40 and 50 km is presented first (V(23/19)z(40/50); Fig. 9). The result for this model at 75 Myr is then compared with other depth-dependent viscosity models at the same time (Fig. 10). The evolution of the topography, plateau coefficient (K_p), and effective width of thickening ($E(t)$), for these models is then compared (Figs 11 and 12) to determine the properties of the lower crust required to produce a plateau.

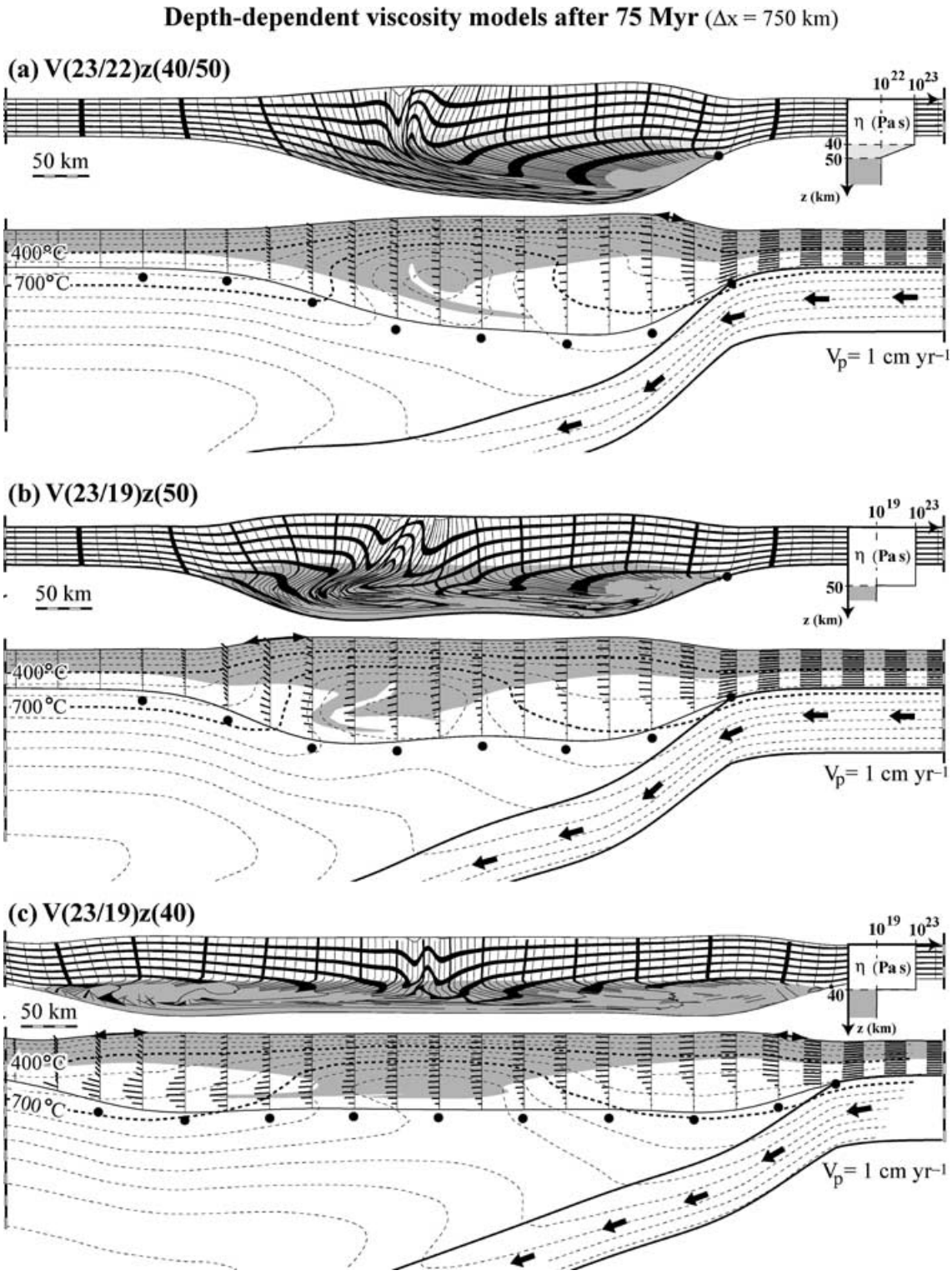

Figure 10. Effect of specific depth dependencies of viscosity. (a) Viscosity decreases linearly by factor of 10 between 40 km and 50 km (model V(23/22)z(40/50)). In this case the result is the double-sloped wedge described in Section 2. In the two other experiments the viscosity decreases by a factor of 10^4 at depth of 50 km (b), model V(23/19)z(40/50), and at 40 km (c), model V(23/19)z(40). See captions Figs 7 and 9 for more details.

The evolution of V(23/19)z(40/50) (Fig. 9) can be compared with that of the equivalent uniform viscosity model UV(23) (Fig. 8). At 15 Myr, the only significant differences are the greater overall symmetry and higher velocities in the lower crust (Fig. 9a). By 45 Myr (Fig. 9b), an embryonic plateau has developed above the thick, low-viscosity lower crustal layer. At 75 Myr (Fig. 9c), these characteristics are more pronounced. The plateau is now 300 km wide and the velocity field in the plateau region indicates pure shear thickening in the upper crust. In the lower crust there is a superimposed symmetric outward flow from beneath the centre of the plateau. Its effect

is to enhance the retro-ward flow beneath the retro-plateau and to diminish the flow beneath the pro-plateau; it is the net retro-ward flow that accounts for retro-ward growth of the plateau.

The geometry and velocity fields (Fig. 9c) are dramatically different from the uniform viscous case (Fig. 8c), which can be understood from the analysis in Section 2. The uniform viscous model corresponds closely to the back-to-back wedge analysis (Fig. 1a), whereas the depth-dependent viscosity model starts with a uniform viscosity but makes the transition to the layered rheology (Fig. 1b); the associated smaller value of F_t beneath the plateau (Fig. 9c vs Fig. 8c) accounts for the much thinner plateau crust.

The thermal evolution of both models is initially similar (Figs 8a and 9a) and is dominated by vertical advection. The thermal structure in the depth-dependent viscosity model is similar at both 45 Myr and 75 Myr, with the plateau underlain by central hot and marginal cool lower crustal regions (Figs 9b and c). In the cool regions, temperatures are low owing to relatively recent vertical advection and subduction cooling. In contrast, the hot region has a keel of radioactive material in the lower crust, and is conductively equilibrated because crustal thickening occurred earlier.

The models (Fig. 10) illustrate the sensitivity of the results to the viscosity decrease and depth range over which it occurs. A value of $\eta_b/\eta_c \sim 0.1$ is not sufficient to create a plateau even after 75 Myr, but leads to an intermediate double-sloped wedge (Fig. 10a, Section 2). Models shown in Figs 10(b) and (c) have step changes in viscosity, with respective z^* values that bound the region of linear variation in V(23/19)z(40/50). The results for V(23/19)z(40/50) and V(23/19)z(50) are similar, showing that models with linear variations in viscosity can be closely reproduced by a step change if z^* is chosen appropriately. Model V(23/19)z(50) has significantly thicker plateau crust than model V(23/19)z(40) (Fig. 10b and c) owing to the larger z^*, although both models have similar plateau geometries ($K_p \sim 0.7$).

The quantitative analysis (Fig. 11) shows the characteristic evolution of the three types of model and the dependence on lower crustal viscosity. The results correspond closely to the predictions of Section 2. The uniform viscosity case, V23, evolves as back-to-back wedges, giving a triangular topography ($K_p \sim 0.5$), progressively thickening crust, and increasing $E(t)$ (Figs 11a, d, e and f). Model V(23/22)z(40/50) represents the double-slope wedge case with steep slopes bounding a low-slope central region (Fig. 11b). The crustal thickness approaches a maximum value (Fig. 11d), even though a true plateau is not created ($K_p < 0.65$, Fig. 11e) and $E(t)$ increases throughout the model evolution (Fig. 11f). Model V(23/19)z(40/50) represents the plateau case (Fig. 11c), having constant $h_{\max}$ for the last 30 Myr of evolution (Fig. 11d), a large $K_p > 0.65$ (Fig. 11e), and a stabilized $E(t)$ (Fig. 11f), all characteristic of plateaux (Appendix A).

The results also illustrate the precursor decreases in $h_{\max}$ and K_p and increase in $E(t)$ (Figs 11c, d, e and f) characteristic of the transition to a plateau. The transition involves a decrease in the early topographic maximum accompanied by retro-ward growth of the wedge and initiation of a retro-edge topographic peak (15–45 Myr, Fig. 11c). Following this transition, the retro- and pro-edge peaks become balanced, with similar heights, and a plateau with no significant surface slope develops between them (45–75 Myr, Fig. 11c). The transition to a plateau does not result from a gradual decrease in surface slope in the central part of the model orogen. Instead, two edge peak barriers are created and the plateau grows between them. The growth of the plateau implies decoupling of the crust from the mantle beneath the plateau, as demonstrated by comparison of models with 10^{20} Pa s $> \eta_b > 10^{18}$ Pa s. All models in this range have similar topography and values of $h_{\max}$, K_p, and $E(t)$; the resemblance to model V(23/19)z(40/50) demonstrates that these models are decoupled and are no longer sensitive to the value of η_b, which is consistent with the predictions in Section 2.

Fig. 12 extends the sensitivity analysis to consider the effect of the critical depth, z^*, on the transition to a plateau. When $\eta_b/\eta_c = 10^{-2}$ (Fig. 12a), $z^* = 40$ km is insufficient to achieve decoupling and the growth of a plateau, whereas, $z^* = 50$ km accomplishes this transition. The result illustrates the inverse dependence of F_{tb} on thickness, h_b, of the weak lower crust (Fig. 1b), in agreement with the predictions, Section 2. Although counter-intuitive, the greater z^* (50 km) leads to decoupling because the larger critical depth results in a thicker crust, a thicker low-viscosity layer, and greater tendency to decoupling and plateau formation (see Section 2). For a large viscosity decrease ($\eta_b/\eta_c = 10^{-4}$, Fig. 12b), the plateau transition occurs even for a thin basal layer. Both models have plateaux because F_{tb} is small owing to the very low η_b, and is no longer sensitive to h_b (Fig. 1b), again in agreement with the analysis, Section 2. A comparison of the evolution of K_p for several models (Fig. 12c) demonstrates that the geometry is relatively insensitive to η_b once the crust is decoupled from the mantle and a plateau is established ($K_p > 0.65$).

5.2 Temperature-dependent viscosity

Temperature-dependent viscosity models were investigated for comparison with the depth-dependent viscosity models, and because temperature controls rheological weakening in natural orogens. It was assumed either that viscosity decreases linearly between 400 and 700°C, corresponding to the range of ductile weakening for crustal rocks, or that there is a step decrease in viscosity at 700°C, coinciding with the onset of partial melting in crustal rocks.

Results from a model in which viscosity decreases from 10^{23} Pa s to 10^{19} Pa s between 400 and 700°C (Fig. 13) can be compared with the approximately equivalent depth-dependent model (Fig. 9). At the largest scale the results are similar. Both models develop plateaux by 75 Myr, even though the viscosity in one case (Fig. 13) is controlled by the temperature, which in both models shows a strong lateral variation beneath the plateau (Figs 9c and 13c), and in the other case by the crustal thickness (Fig. 9). Evidently, it makes little difference to plateau evolution whether the low-viscosity basal layer is thick, as it is below the retro-plateau, or thin, as it is more pro-ward (Fig. 13c), provided the basal traction, F_{tb}, is small enough. This result implies that the crust beneath plateaux need not be compositionally, structurally, or thermally homogeneous, it only needs a sufficiently weak base, as predicted in Section 2.

At smaller scales there are differences between the models. The retro-ward propagation of the plateau is more efficient in the depth-dependent viscosity model because viscosity decreases as the crust thickens. In the temperature-dependent viscosity model, temperature must first increase and there is a corresponding delay in the outward crustal flow. This difference accounts for the temperature inversion beneath the retro-plateau (Fig. 13c), the different velocity variations with depth, and the different crustal thickening styles (Figs 9c and 13c).

Results from other models with temperature-dependent viscosities (Fig. 14) show that a decrease in viscosity from 10^{23} to 10^{22} Pa s is not sufficient to create a true plateau (Fig. 14a). The basal traction remains high beneath the pro-ward side of the plateau where a relatively thin region of the basal crust exceeds 700°C. The overlying crust has wedge characteristics. Fig. 14(b) illustrates the result from

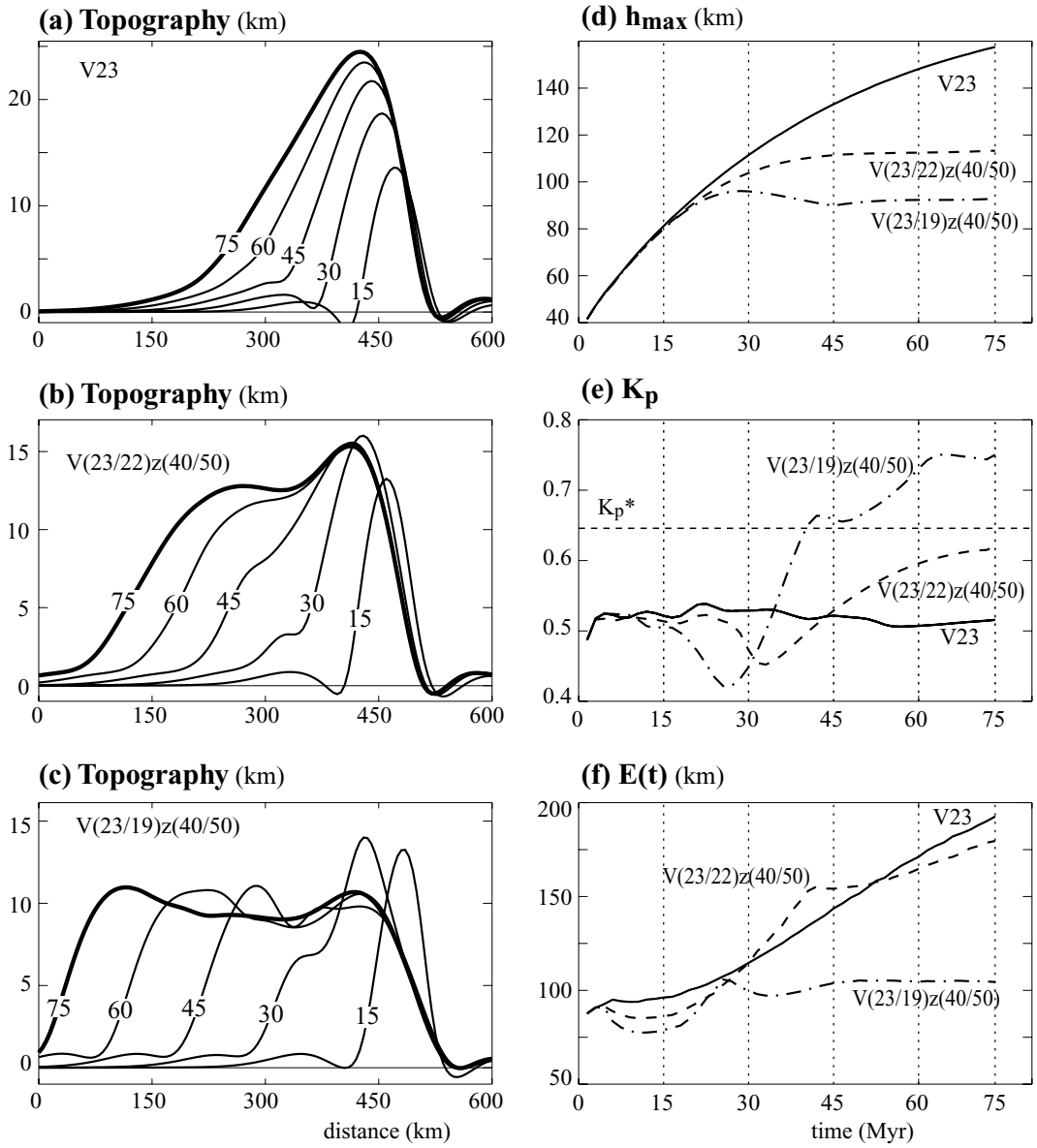

Figure 11. Geometric evolution of model orogens with uniform (V23, see also Fig. 8), and depth-dependent viscosity (V(23/22)z(40/50), see also Fig. 10a; and V(23/19)z(40/50), see also Fig. 9). These three models differ only in terms of basal viscosity. (a)–(c) Topography at 15, 30, 45, 60, 75 Myr, S at $x =$ 500 km. (d)–(f) Evolution of integrated parameters: $h_{\max}$, maximum thickness of the crust, *Kp*, plateau coefficient (the critical value used to define a plateau-like structure is marked by *Kp*∗), and, $E(t)$, effective width of thickening. See Appendix A for details.

model FP(15)-V23/19)T(400/700), which is the same as that shown in Fig. 13(c) except that the viscous stresses are limited by frictional–plastic stresses ($\phi = 15^\circ$). Generally, at high strain rate, the upper part of the model behaves like the corresponding frictional–plastic case, while lower strain rates result in viscous behaviour. The similarity of the results at 75 Myr (Figs 13c and 14b) suggests that the dominant rheology is viscous in both cases, reflecting low deformation rates in the upper crust during the later, plateau stage of model evolution. The early evolution of these models resembles the uniform rheology models (Section 4.3, Figs 7 and 8).

The topographic evolution of the temperature-dependent viscosity models (Fig. 15) may be compared with that of the approximately equivalent depth-dependent viscosity model (Fig. 11). The comparison confirms the similarity of the orogen-scale topographic evolution and the evolution of the integrated geometrical parameters. The main difference between the two types of models is that the temperature-dependent viscosity models with the rheological transition between 400 and 700°C are pre-weakened (viscosity is 2–4×10^{22} Pa s at the base of the crust where the temperature is higher than 400°C, the lower limit of the rheological transition), leading to minor differences in early model evolution. Despite this initial weakening, the basal viscosity is sufficiently high that the temperature-dependent viscosity models all behave as viscous wedges during their first 20 Myr.

The models presented so far were chosen to produce thick plateau crust and high topography in order to emphasize characteristic properties. Fig. 16 shows the sensitivity of plateau elevation and corresponding crustal thickness to variations in the radioactive heat production of the model crust. Uniform radioactivity $A_2 = 0.4$ μW m^{-3} is introduced in the lower crust in one model (dashed line,

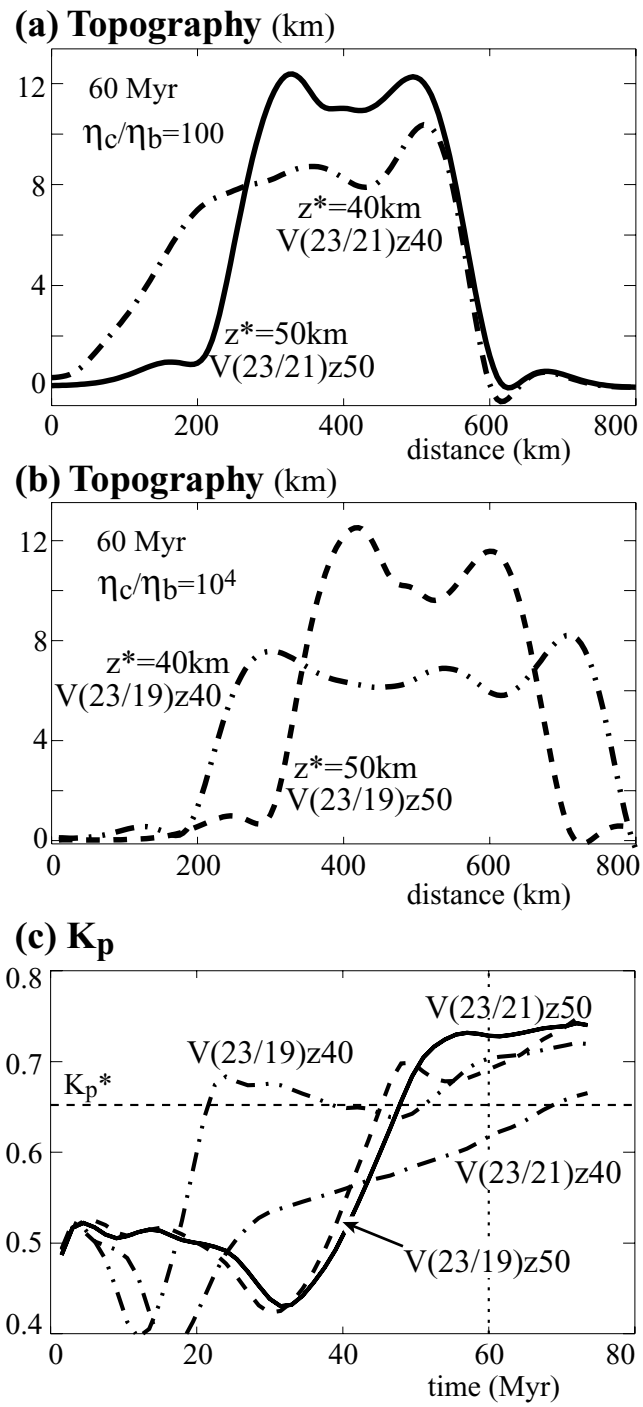

Figure 12. Results for depth-dependent models with different viscosity profiles. (a) Topography at 60 Myr for models with the same ratio $\eta_b/\eta_c = 10^{-2}$, but different depth of transition: V(23/21)z(50) (solid line) and V(23/21)z(40) (dash-dot line). (b) Topography at time 60 Myr for models with the same ratio $\eta_b/\eta_c = 10^{-4}$, but different depth of transition: 50 km, V(23/19)z(50) (dash line) and 40 km, V(23/19)z(40) (dash-dot-dot line). (c) Evolution of plateau coefficient for the models presented in (a) and (b).

Fig. 16), and in a second model the viscosity of the upper crust is also reduced by a factor of two (dash-dot line, Fig. 16). The increase in radioactive self-heating is offset by a decrease in the basal heat flux in order to maintain the same surface heat flux as other models. The effect is to produce model plateau elevations that approach observations from Tibet and the Altiplano (ca. 5500 m). The important conclusion is that model plateau elevation and crustal thickness are sensitive to the choice of upper crustal viscosity, and secondarily to the distribution and amount of crustal radioactivity. Reducing the upper crustal viscosity by a factor of three to ca. 3×10^{22} Pa s is all that is required to produce more natural-looking plateaux.

5.3 Thermal evolution of a temperature-dependent viscosity model

Model V(23/19)T(700), in which there is a step decrease in viscosity from 10^{23} to 10^{19} Pa s at 700°C, is used for a more detailed assessment of thermal evolution and its consequences (Fig. 17). The average crustal viscosity for this model is higher than that of V(23/19)T(400/700) (Fig. 13); the model orogen is therefore narrower and thicker at 75 Myr, but otherwise has similar characteristics.

The temperature at the base of the crust (T_{Moho}) exerts a fundamental control on basal traction, and thus on model evolution. T_{Moho} evolves in two phases (Fig. 17c). For $t < 30$ Myr, T_{Moho} increases in the vicinity of S and decreases on the retro-side where the temperature field is subjected to vertical stretching above the subducting slab (see Section 2). By 45 Myr, $T_{\mathrm{Moho}} > T^* = 700$°C across a significant zone retro-ward of S, leading to basal decoupling and the onset of the transition to a plateau. The second phase ($t > 45$ Myr) corresponds to the progressive retro-ward migration of the increasing temperature maximum, growth of the region of thick crust, and the creation of a plateau.

The relationship of T_{Moho} to the thickening of the crust, particularly the radioactive layer, can be assessed for the central part of the orogen (region between dashed lines, Fig. 17c). For $t < 30$ Myr the vertical stretching of the temperature field above the subducting slab dominates and T_{Moho} decreases even though h_r increases (Fig. 17d). Between 35 and 60 Myr T_{Moho} and h_r increase together. After 60 Myr a plateau has formed and the orogen now widens rather than thickens. Therefore, the advective cooling caused by the vertical stretching of the temperature field in the crust ends, allowing T_{Moho} to increase even though h_r does not. The increase in T_{Moho} is enhanced by the keel of deeply buried radioactive crust (Fig. 17a). Growth of this keel as the thickened crust is translated retro-ward contributes to the progressive increase of T_{Moho} beneath the retro-plateau for $t > 45$ Myr.

The temperature structure in the crust reflects competition among heat production (R), advection during vertical stretching (A), and conduction (C), as shown in Fig. 17(e) for the centre of the orogen (Figs 17a and b). Consider the relative effects of these components as the crust actively thickens between 30 Myr and 75 Myr (Fig. 17d). The initial ($t = 30$ Myr) geotherm T_{30} is advected downward to T_A by vertical stretching alone. The added effect of heat production increases temperature to T_{A+R}; the two thermal peaks stem from the upper crust and keel regions. Conduction diffuses the temperature field and heat is lost at the surface, leading to the final geotherm $T_{A+R+C} = T_{75}$ at 75 Myr (Fig. 17e, bold line). Middle to upper crustal temperatures mainly reflect heat production and conduction, whereas the lower crust still retains the effect of advection. There is a small temperature inversion (larger at the retro-margin of the plateau, Fig. 17b) and T_{Moho} is lower than the initial geotherm projected to the same depth (Fig. 17e). These effects combine to produce a crustal temperature regime that is far from conductive steady-state and a nearly isothermal lower crust with $T \sim 800$–900°C.

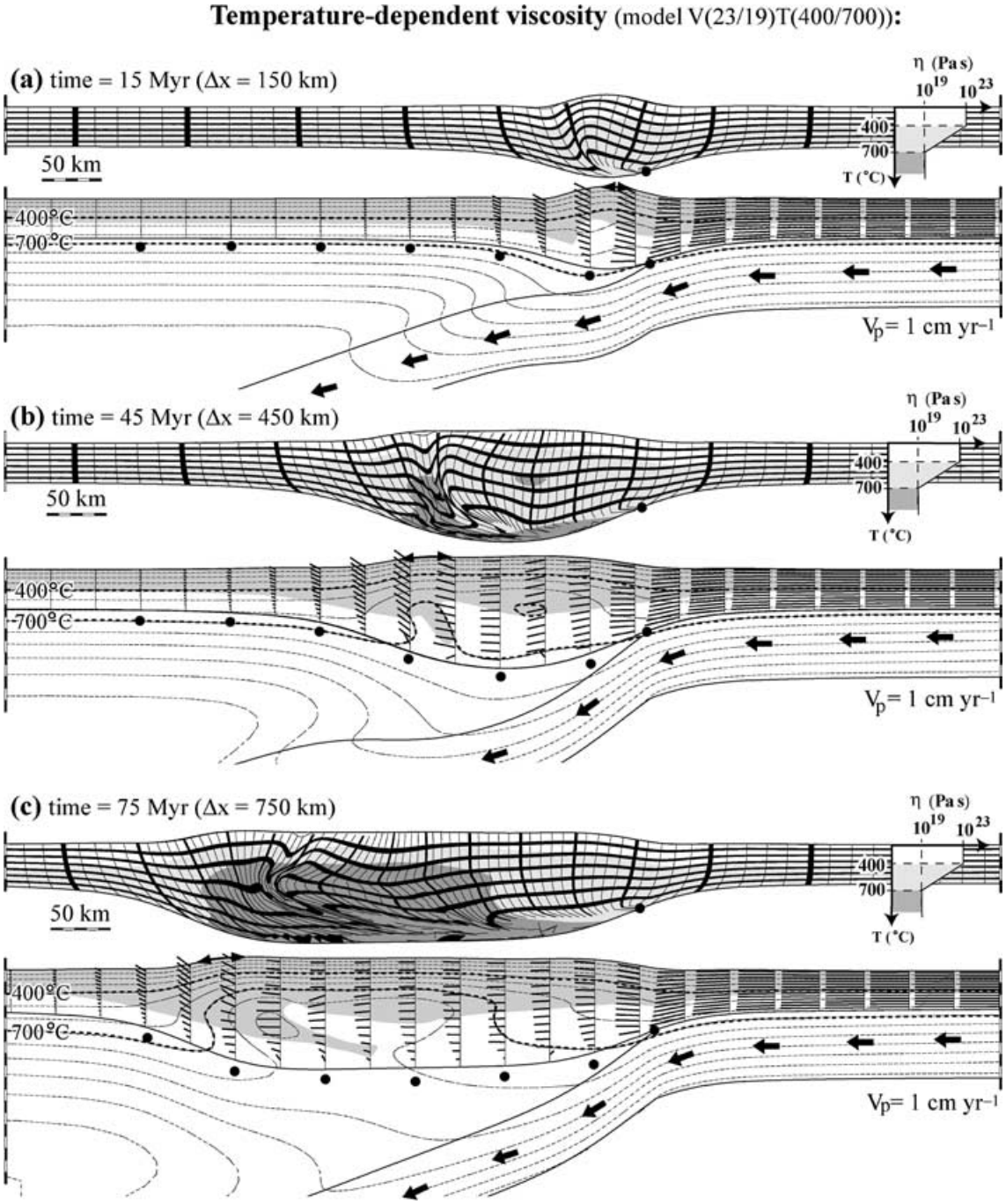

Figure 13. Evolution of model V(23/19)T(400/700) with temperature-dependent viscosity. The design is similar to Fig. 9, except that the rheological transition depends on temperature. Results are shown after (a) 15 Myr, (b) 45 Myr and (c) 75 Myr.

A major difference between depth- and temperature-dependent models can occur in the magnitude of F_{tc} (Fig. 1b) which acts to couple the wedges bounding the plateau to underlying mantle lithosphere. As shown by the scale analysis (Fig. 1b) F_{tc} depends on z^* and the length scale over which the coupling is strong. In models with depth-dependent rheologies (Section 5.1) the z^* chosen, 40–50 km, limits the size of the bounding wedges, and therefore the size of F_{tc} and the thickness of the plateau crust. However, in the temperature-dependent models vertical advection of the thermal field in the bounding wedges (e.g. Figs 13c and 17b) can increase z^* significantly with respect to its initial value, z_{init}, in the undeformed lithosphere (e.g. Fig. 17f, $z^* \sim 75$ km, $z_{\text{init}} \sim 40$ km). The coupling length scale correspondingly increases and therefore the plateau crust is much thicker. The effective value of z^* (Fig. 17f) is relatively stable in model V(23/19)T(700) and therefore the thickness of the plateau crust changes little as the plateau widens. In general, however, the thickness of the plateau crust is sensitive to the thermally determined z^* in the bounding wedges. Therefore the

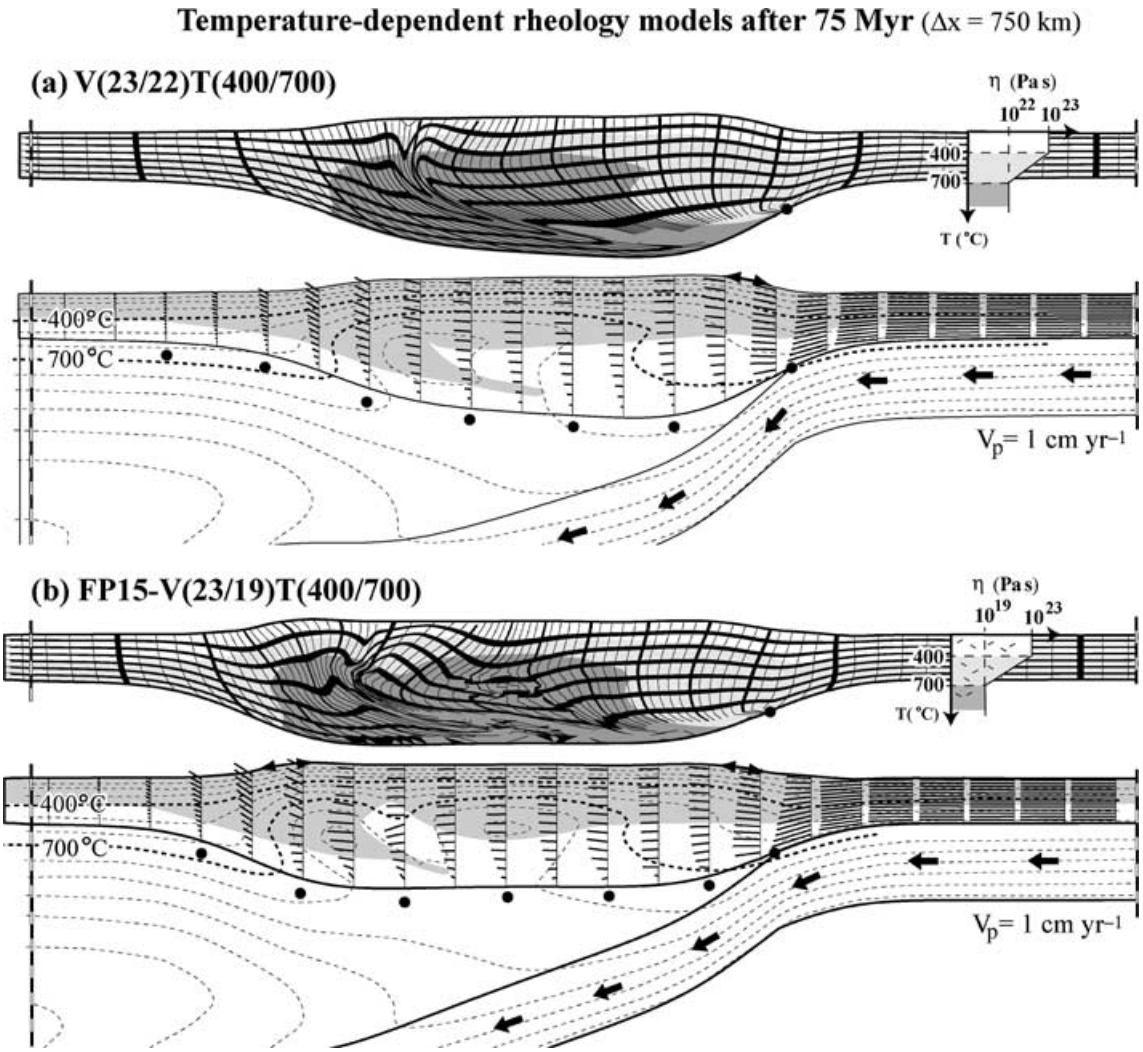

Figure 14. Effect of different temperature-dependent rheologies on models after 75 Myr of convergence. (a) Model V(23/22)T(400/700) in which viscosity decreases by a factor of 10 between 400°C and 700°C. Note a decrease of the surface slope above the weak basal layer but no transition to a plateau. (b) Model FP(15)-V(23/19)T(400/700) is characterized by a visco-plastic rheology, viscosity decreases from 10^{23} Pa s to 10^{19} Pa s between 400°C and 700°C. The rheology has a frictional–plastic cap, $\phi = 15°$, and cohesion of 10^6 Pa. Schematic rheology profile only depicts the viscous component. See caption Fig. 9 for other details.

choice of the thermal model parameters and the convergence velocity can strongly influence the thickness of plateau crust and the plateau height.

6 DISCUSSION

Comparison among the models provides some insights into the influence of simple rheologies on orogenesis and the extent to which the basic properties of orogens can be approximated with simple rheologies and the mantle subduction model. These results should be compared and contrasted with the models based on distributed whole lithosphere pure shear deformation listed in the introduction. The models also begin to address the validity of the 'depth-dependent' assumption for the viscosity within orogenic crust or, alternatively, whether the viscosity should be related to a more complete calculation of the thermal evolution. The models are, however, only simple approximations of natural orogens and they are not designed for comparison with particular orogens. Specific applications to large hot orogens with plateaux (Beaumont *et al.* 2001a,b; Jamieson *et al.* 2002) use models that are based on those presented here but employ frictional–plastic and thermally-activated power-low creep rheologies and include surface denudation and the approximate large-scale effects of crustal melting. Such models have applications to the Himalayan-Tibet orogen (Beaumont *et al.* 2001a,b) and possibly to the Altiplano, the Grenvillian orogen and the Western Canadian Cordillera (see Pope & Willett 1998). However, the complexity of these models tends to obscure some of the basic properties that are best derived from the simple models presented here.

When the crust is subject to uniform velocity subduction basal boundary conditions with a fixed subduction location, a crustal layer with uniform viscous or frictional–plastic properties deforms to create bivergent back-to-back tectonic wedges with no limit in size. These wedges may undergo near-surface instantaneous extension, expressed as extensional strain rate, but the crust continues to thicken and the wedges continue to grow, in accordance with results from analogue (Buck & Sokoutis 1994) and numerical (Willett *et al.*

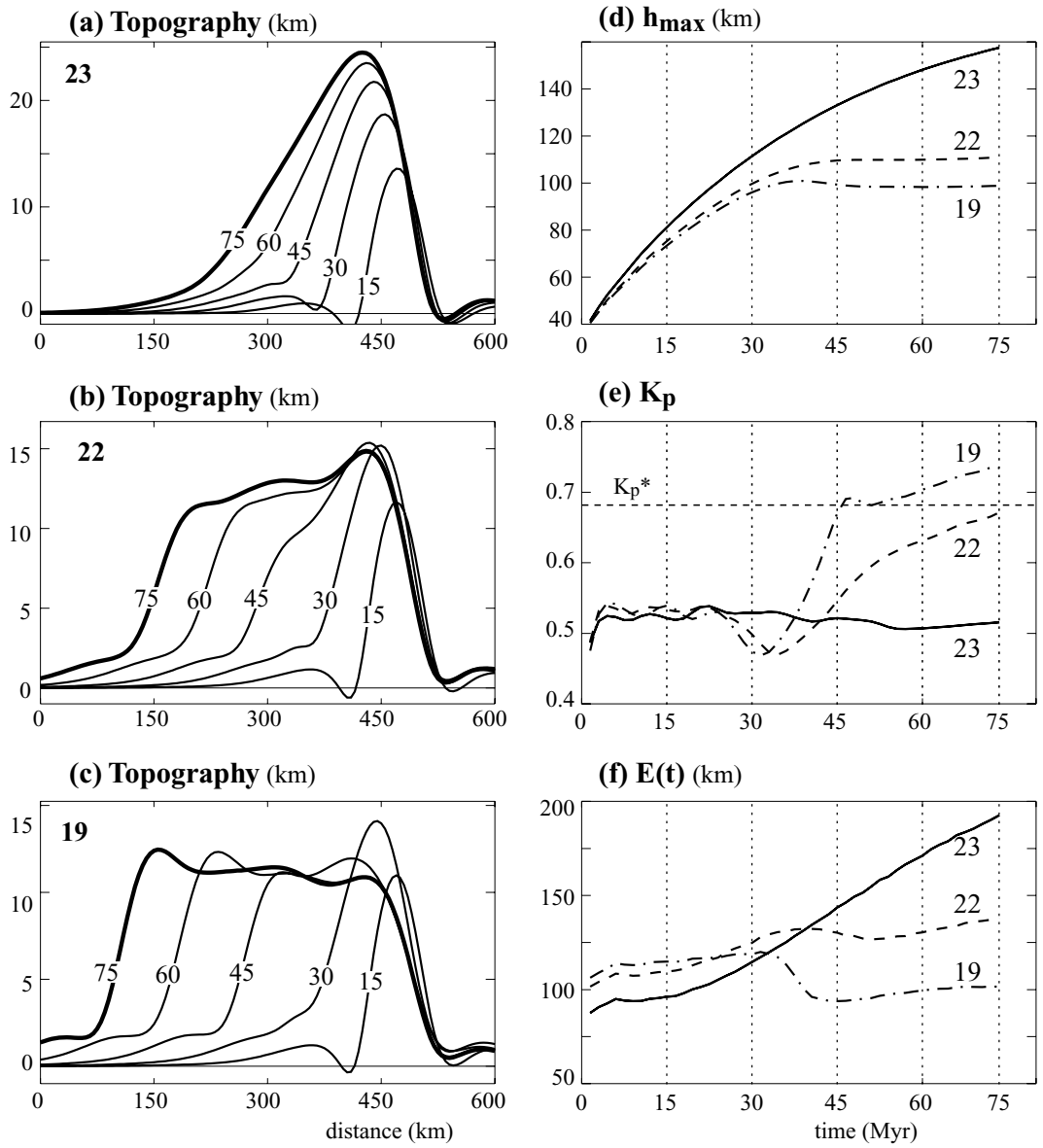

Figure 15. Geometrical evolution of models with uniform (V23, see also Figs 8 and 11), and temperature-dependent viscosity: V(23/22)T(400/700) (see also Fig. 14a) and V(23/19)T(400/700) (see also Fig. 13). These three models differ only by one parameter, the basal viscosity η_b. For details see caption Fig. 11.

1993; Royden 1996; Willett 1999) models. The overall behaviour can be analysed using the force balance (Section 2) in which horizontal compression and gravity oppose the basal traction.

In a frictional–plastic crust, convergence is accommodated by plug uplift and the growth of bounding wedges that increase their tapers until a critical value is achieved (Davis *et al.* 1983; Dahlen *et al.* 1984). Further growth occurs at these tapers and the behaviour is characterized by Rm_ϕ (Fig. 5, see also Willett 1999). Near-surface instantaneous extension coeval with convergence can occur if underthrusting beneath the wedge increases the taper and causes extensional failure (Platt 1986).

A viscous crust initially responds by dominantly local thickening and vertical growth governed by the competition between basal traction and horizontal viscous compressional forces. Later, as the wedges thicken, lateral gradients in gravitational potential energy increase the forces driving lateral spreading. At this stage wedge evolution is characterized by Rm (Figs 1a and 5). Near-surface extension occurs when viscous relaxation exceeds contraction (Willett 1999; Medvedev 2002).

In subduction-driven models, the formation of a plateau requires a decrease in basal traction. This is achieved in the present models by a reduction of strength with depth or temperature. Royden (1996) and Shen *et al.* (2001) reached the same conclusion based on models with depth-dependent viscosities and basal velocity boundary conditions. In contrast, models in which it is assumed that velocity does not vary with depth are overconstrained because strain cannot be partitioned with depth. Such models (e.g. England & Houseman 1988) actually predict that lithospheric weakening leads to local thickening. In the current models, a reduction in the viscosity ratio, $\eta_b/\eta_c \sim 10^{-2}$, is sufficient to cause the transition from wedge to plateau, but this transition also depends on h_b (Fig. 1b) because it is the basal traction, F_{tb}, that must decrease beneath the plateau. Further reduction of the viscosity ratio has no additional influence on the models because the plateau is now decoupled from the basal traction and the behaviour

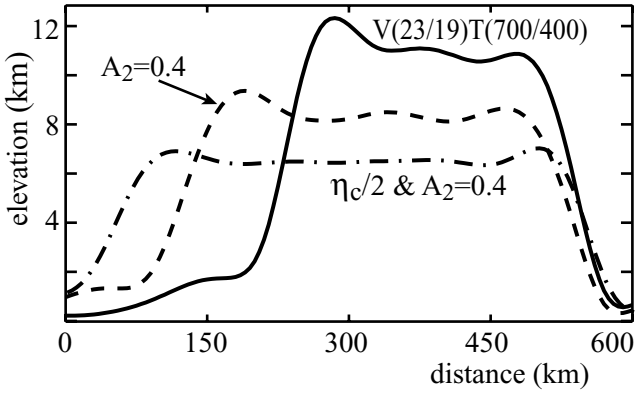

Figure 16. Sensitivity of plateau elevation at 60 Myr to radioactivity in the lower crust and to the decrease in viscosity of the upper crust. The reference model V(23/19)T(400/700) (solid line, see also Fig. 13) is compared with a similar model with radioactive heat production $A_2 = 0.4\ \mu$W m^{-3} in the lower crust (dashed line), and to the model with $A_2 = 0.4\ \mu$W m^{-3} and upper crustal viscosity reduced by a factor of 2 (dash-dot line).

is governed by the relation between F_{tc} and F_g (Fig. 1b), which no longer depends on η_b and h_b.

The model results also provide information on the form of the transition from wedge to plateau, showing, for example through the evolution of K_p and $E(t)$, that a wedge geometry is initially preserved despite the development of a significant amount of lower-crustal low viscosity material. A plateau does not develop at the onset of basal weakening, but instead the model evolves through the double-wedge phase before full basal decoupling is achieved. In some models, the transition is also accompanied by significant thinning of previously thickened crust, which is interpreted as a release of potential energy which cannot be sustained when the basal traction decreases. Plateau-edge topographic peaks are a feature of the numerical models and are also expected to occur in nature (Medvedev *et al.* 2000). They are spatially correlated with places where the basal boundary condition, or traction, changes abruptly from coupled to decoupled and the converse. Models of ice streams (Barcilon & MacAyeal 1993) show a similar decrease in topography across the transition from no-slip to free-slip on their base, suggesting that the topographic variation is linked to large lateral variations in effective viscosity (Medvedev *et al.* 2000).

Under what circumstances is the use of depth as a proxy for temperature valid in the study of model orogens, and in particular in analysing the wedge-plateau transition? This assumption, used for example by Royden (1996) and Shen *et al.* (2001), appears unrealistic when the thermal structure of the crust departs strongly from a vertical conductive equilibrium, as it does in all of the models presented here. Most models (e.g. Figs 9b, c, 10, 13c and 14) have large lateral contrasts in their temperature fields between the pro- and retro-plateau crusts. Consequently, the evolving viscosity structure differs dramatically from that predicted by a model with a depth-dependent viscosity calibrated to give the same initial viscosity structure. The question can be answered at two levels—in terms of the large-scale model geometry, and in terms of the finer internal structure of the plateau crust.

At a large scale, the model geometries of some depth-dependent and temperature-dependent models (e.g. V(23/19)z(40/50), Fig. 9; V(23/19)T(400/700), Fig. 13) are more alike than their viscosity structures suggest. This holds where both parametrizations predict full decoupling of the lower crust from the basal traction and, therefore, little sensitivity to the viscosity ratio η_b/η_c, or h_b and its lateral variation. In particular, the four orders in magnitude decrease in viscosity with depth and the thickness of the weak basal layer guarantee that both approaches yield similar first-order results. The differences would be much greater if the viscosity decrease was only one order of magnitude. In summary, once a plateau exists, its geometry is only weakly dependent on the viscosity distribution within the plateau crust. This does not demonstrate the validity of the depth-dependent viscosity model, it only indicates that under these limiting conditions, both approaches yield similar results.

At the finer scale, the velocity and deformation fields of the depth- and temperature-dependent models do differ, particularly beneath the central/retro-plateau where the viscosity distributions are quite different (e.g. Figs 9 and 13). For example, retro-ward extrusion is confined to the lower crust in the depth-dependent model but is more distributed in the temperature-dependent model. Other properties such as metamorphic facies distributions, regions of partial melting, and surface heat flux would, however, be similar for both models.

The thermal evolution of both depth- and temperature-dependent models that form plateaux is similar and can be described in terms of the back-to-back wedge and plateau phases. The analysis presented in Section 2 indicates how the heat balance will differ between the two phases. For the parameter values used here, all three components of the heat balance (advection, conduction, and radioactive self-heating) are important during the first orogenic phase. This is dominated by crustal thickening and subduction, which imply that vertical advection of heat and increased vertically integrated radioactive self-heating strongly perturb the steady-state conductive regime (Fig. 17). The thermal effects of crustal thickening remain important in the bounding wedges during the second orogenic phase. However, beneath the plateau, thickening and vertical advection cease within the crust, the rate of radioactive self-heating becomes constant, and the crust thermally relaxes toward a new steady state. Horizontal advection of heat is now important because at the largest scale the plateau crust is transported retro-ward as the plateau grows. The thermal regime of the plateau crust can therefore be divided into three main regions, the cold retro- and pro-plateau flanks where recently thickened crust has not had time to thermally relax, and the older, hot central plateau that is thermally relaxed.

The numerical model results generally confirm the thermal scale analysis described above. The main difference is caused by heterogeneous crustal thickening during phase one. The resulting keels of radioactive upper crust buried in the lower crust augment the effect of radioactive self-heating in the central part of the plateau (e.g. Figs 9, 10, 13 and 14). This heterogeneous thickening occurs in all models that are driven by basal subduction and that are initially coupled to the basal traction.

7 CONCLUSIONS

For the boundary conditions and parameters used in these models (Table 1), including basal subduction at constant velocity, V_p, and simple frictional–plastic and viscous rheologies, we can draw the following conclusions concerning the controls on orogenic wedges and plateaux and the transition between them.

(1) Deformation of crustal layers with constant rheologic behaviour (frictional–plastic or constant viscous) leads to the growth of back-to-back wedges with no limit in crustal thickness. Wedge taper is inversely dependent on Rm: increasing V_p or η_c, decreasing ρ_c (viscous wedges), or increasing ϕ (frictional–plastic wedges), produces narrower and thicker wedges. The taper evolves with time

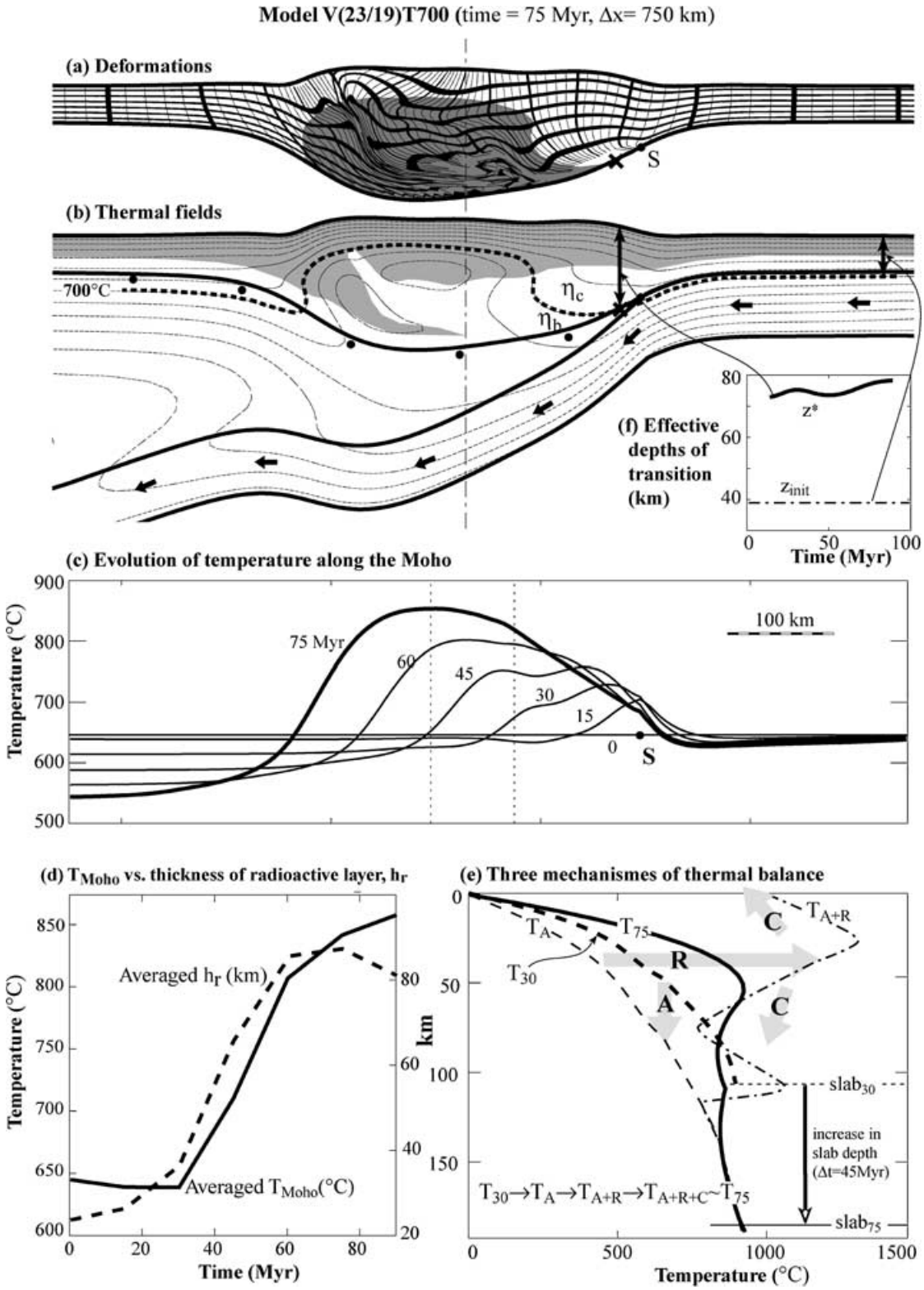

Figure 17. (a) Deformation and (b) thermal-rheological fields for model V(23/19)T(700) at 75 Myr. The rheological transition is set at temperature $T^* =$ 700°C and a black cross marks where the transition temperature crosses the Moho giving an effective z^*. (c) Evolution of Moho temperature from 0 to 75 Myr. (d) Evolution of Moho temperature and thickness of the radioactive layer, averaged over 100 km around dashed line indicated in (a). (e) Illustration of the way in which radioactive self-heating (R), advection (A) and conduction (C) contribute to the thermal evolution along the dashed line indicated in (a) from the top surface to the upper surface of the subducting slab. T_{30} is the geotherm at 30 Myr (when deformation reached this region) and T_{75} is the geotherm at 75 Myr. Evolution of the profile with time is illustrated using three parts of thermal balance (Fig. 2): Advection (A) stretches the profile T_{30} to T_A (owing to the increase in depth of slab); radioactive heating (R) increases the temperature inside the radioactive layer to T_{A+R} (note two peaks of profile reflect the shape of radioactive layer); conduction (C) smoothes the profile so that $T_{75} \sim T_{A+R+C}$. (f) Time variation in the effective depth, z^*, of transition (i.e. the depth of T^* where it crosses the Moho in (b)), showing that owing to vertical advection it is much larger than the initial depth of T^*, z_{init}.

for viscous models, while in frictional–plastic models, critical taper, once achieved, is maintained.

(2) Models that are characterized by a decrease in crustal viscosity from η_c to η_b with depth or temperature, leading to partial or full basal decoupling, display more complex behaviour. For models with moderate η_b/η_c, the crustal wedges have dual tapers with a lower taper in the central region and a higher taper on the edges of the deformed crust. A viscosity ratio $\eta_b/\eta_c \sim 10^{-2}$ is sufficient to cause the transition from wedge to plateau, but this transition also depends on h_b because of the effect of basal traction.

(3) Values of $\eta_b/\eta_c \sim 10^{-4}$ lead to plateaux in all cases because the lower crust is now fully decoupled from the basal traction. In these cases, large-scale model geometries for both depth- and temperature-dependent rheologies are similar and gravity-driven flow is concentrated in the low viscosity region. In most models, the plateaux grow laterally at constant thickness between characteristic edge peaks which are probably associated with the transitions from coupling to decoupling beneath the plateau flanks.

(4) Except beneath the central region of a mature plateau, the models depart significantly from conductive steady-state, with strong lateral temperature gradients controlled by the interaction of horizontal and vertical thermal advection, diffusion, and heterogeneous thickening of the radioactive crustal layer. These lead to differences in the velocity and deformation fields between models with depth- vs. temperature-dependent rheologies, particularly at the plateau margins. Although simple depth-dependent viscosity models may be reasonable approximations for describing the large-scale geometry of fully developed plateaux, they are not appropriate for describing the internal features of large orogenic systems or the transition from wedge to plateau geometry.

ACKNOWLEDGMENTS

This research was funded by NSERC Research and Lithoprobe Supporting Geoscience grants to CB and RAJ, and the Inco Fellowship of the Canadian Institute for Advanced Research to CB. We thank editor Harro Schmeling, Peter Bird and Susanne Buiter for their careful and useful reviews of the early version of the manuscript.

REFERENCES

Barcilon, V. & MacAyeal, D.R., 1993. Steady flow of a viscous ice stream across a no-slip/free-slip transition at the bed, *J. Glaciol.,* **399,** 167–185.

Batt, G.E. & Braun, J., 1997. On the thermomechanical evolution of compressional orogens, *Geophys. J. Int.,* **128,** 364–382.

Beaumont, C., Jamieson, R.A., Nguyen, M.H. & Lee, B., 2001a. Himalayan tectonics explained by extrusion of a low viscosity crustal channel coupled to focused surface denudation, *Nature,* **414,** 738–742.

Beaumont, C., Jamieson, R.A., Nguyen, M.H. & Lee, B., 2001b. Mid-crustal channel flow in large hot orogens: results from coupled thermal–mechanical models, in *Slave-Northern Cordillera Lithospheric Evolution (SNORCLE) and Cordillerian Tectonics Workshop; Report of 2001 Combined Meeting,* Vol. 79, pp. 112–170, eds Cook, F. & Erdmer, P., Lithoprobe Report, Lithoprobe Secretariat, Department of Geological Sciences, University of British Columbia, Canada.

Bird, P., 1989. New finite-element technique for modelling deformation histories of continents with stratified temperature-dependent rheology, *J. geophys Res.,* **94,** 3967–3990.

Bird, P., 1991. Lateral extrusion of lower crust from under high topography, in the isostatic limit, *J. geophys Res.,* **96,** 10 275–10 286.

Buck, R.W. & Sokoutis, D., 1994. Analogue model of gravitational collapse and surface extension during continental convergence, *Nature,* **369,** 737–740.

Chapple, W.M., 1978. Mechanics of thin-skinned fold-and-thrust belts, *Bull. GSA,* **89,** 1189–1198.

Dahlen, F.A., 1984. Non-cohesive critical Coulomb wedges: an exact solution, *J. geophys Res.,* **89,** 10 125–10 133.

Dahlen, F.A., Suppe, J. & Davis, D., 1984. Mechanics of fold-and-thrust belts and accretionary wedges: Cohesive Coulomb theory, *J. geophys Res.,* **89,** 10 087–10 101.

Davis, D., Suppé, J. & Dahlen, F.A., 1983. Mechanics of fold-and-thrust belts and accretionary wedges, *J. geophys Res.,* **88,** 1153–1172.

Ellis, S., Fullsack, P. & Beaumont, C., 1995. Oblique convergence of the crust driven by basal forcing: implications for length-scales of deformation and strain partitioning in orogens, *Geophys. J. Int.,* **120,** 24–44.

England, P.C. & Houseman, G.A., 1988. The mechanics of the Tibetan Plateau, *Phil. Trans. R. Soc. Lond., A.,* **326,** 301–320.

England, P.C. & McKenzie, D.P., 1982. A thin viscous sheet model for continental deformation, *Geophys. J. R. astr. Soc.,* **70,** 292–321.

England, P.C. & Thompson, A.B., 1984. Pressure-Temperature-time paths of regional metamorphism I. Heat transfer during the evolution of regions of thickened continental crust, *J. Petrol.,* **25,** 894–928.

Fielding, E., Isacks, B.L., Barazangi, M. & Duncan, C., 1994. How flat is Tibet?, *Geology,* **22,** 163–167.

Fullsack, P., 1995. An arbitrary Lagrangian-Eulerian formulation for creeping flows and its application in tectonic models, *Geophys. J. Int.,* **120,** 1–23.

Henry, P., Le Pichon, X. & Goffé, B., 1997. Kinematic, thermal and petrological model of the Himalayas: constraints related to metamorphism within the underthrust Indian crust and topographic elevation, *Tectonophysics,* **273,** 31–56.

Houseman, G.A. & England, P.C., 1986. Finite strain calculations of continental deformation 1. Method and general results for convergent zones, *J. geophys Res.,* **91,** 3651–3663.

Houseman, G.A., McKenzie, D.P. & Molnar, P., 1981. Convective instability of a thickened boundary layer and its relevance for the thermal evolution of continental convergent belts, *J. geophys Res.,* **86,** 6115–6132.

Huerta, A.D., Royden, L.H. & Hodges, K.V., 1996. The interdependence of deformational and thermal processes in mountain belts, *Science,* **273,** 637–639.

Jamieson, R.A., Beaumont, C., Fullsack, P. & Lee, B., 1998. Barrovian regional metamorphism: Where's the heat?, in *What Drives Metamorphism and Metamorphic Reactions? Special Publication 138,* pp. 23–51, eds Treloar, P.J. & O'Brien, P.J., Geological Society, London.

Jamieson, R.A., Beaumont, C., Nguyen, M.H. & Lee, B., 2002. Interaction of metamorphism, deformation and exhumation in large convergent orogens, *J. metamorph. Geol.,* **20,** 9–24.

Medvedev, S., Beaumont, C., Vanderhaeghe, O., Fullsack, P. & Jamieson, R.A., 2000. Evolution of continental plateaux: Insights from thermal–mechanical modelling., San Francisco, USA, *EOS, Trans. Am. geophys. Un.,* **81,** F1094.

Medvedev, S., 2002. Mechanics of viscous wedges: Modelling by analytical and numerical approaches, *J. geophys Res.,* **107,** 10.1029/2001JB000145,ETG pp. 9 1–15.

Neil, E.A. & Houseman, G.A., 1997. Geodynamics of the Tarim basin and the Tien Shan in Central Asia, *Tectonics,* **16,** 571–584.

Pope, D.C. & Willett, S.D., 1998. thermal–mechanical model for crustal thickening in the Central Andes driven by ablative subduction, *Geology,* **26,** 511–514.

Royden, L., 1996. Coupling and decoupling of crust and mantle in convergent orogens: Implications for strain partitioning in the crust, *J. geophys Res.,* **101,** 17 679–17 705.

Shen, F., Royden, L.H. & Clark, B.B., 2001. Large-scale crustal deformation of the Tibetan Plateau, *J. geophys. Res.,* **106,** 6793–6816.

Sonder, L.J., England, P.C., Wernicke, B.P. & Christiansen, A., 1987. A physical model for Cenozoic extension of western North America, in *Continental Extensional Tectonics*, *Special Publication*, pp. 187–201, eds Coward, M.P., Dewey, J.F. & Hancock, P.L., Geological Society, London.

Thompson, A.B. & Connolly, J.A.D., 1995. Melting of the continental crust: Some thermal and petrological constraints on anatexis in continental collision zones and other tectonic settings, *J. geophys Res.,* **100,** 15 565–15 579.

Vanderhaeghe, O., Beaumont, C., Fullsack, P., Medvedev, S., & Jamieson, R.A., 1998. thermal–mechanical modelling of convergent orogens: the

role of rheology, isostasy and temperature, in *ECSOOT Transect Meeting, UBC,* Vol. 73, pp. 44–85, eds Wardle, R. & Hall, J., Lithoprobe Report.
Willett, S., Beaumont, C. & Fullsack, P., 1993. Mechanical model for the tectonics of doubly vergent compressional orogens, *Geology,* **21,** 371–374.
Willett, S.D., 1999. Rheological dependence of extension in wedge models of convergent orogens, *Tectonophysics,* **305,** 419–435.

APPENDIX A: QUANTITATIVE DEFINITION OF A PLATEAU

A1 Geometrical characteristics: the plateau coefficient, $K_p(t)$

We define a perfect plateau as a region of significant surface uplift with perfectly flat topography and vertical sides. In 2-D, the perfect plateau equivalent of a region of high topography (grey, Fig. A1a) is a rectangle (dashed line, Fig. A1a) with height, h_p, equal to 80 per cent of the maximum elevation and width, λ_p, equal to the width of the highland within the 80 per cent region. The lowest 20 per cent of the elevated region, $w(x, t) \neq 0$, is not considered to avoid the possible influence of small topographic variations outside the main orogenic structure. The plateau coefficient, $K_p(t)$, is defined as the ratio of the cross-sectional area of the elevated region, A_t (shaded on Fig. A1a), to the cross-sectional area of the corresponding perfect plateau, A_p, multiplied by the geometrical factor, r (Fig. A1a). r should be close to 1 when $\lambda_p \gg h_p$, in keeping with the view that plateaux are much wider than they are high.

A perfect plateau has $K_p = 1$, and triangular back-to-back wedges have $K_p \sim 0.5$. The value of K_p is not very sensitive to the choice of the cut-off percentage used to define the perfect plateau. Natural plateaux, including the Tibetan plateau (Fielding *et al.* 1994; Neil & Houseman 1997) have $K_p \sim 0.8$.

Fig. A1(b) shows the evolution of $K_p(t)$ for models with depth-dependent rheologies with different values of basal viscosity. The uniform viscous model ($\eta_c = \eta_b = 10^{23}$) has $K_p(t) \sim 0.5$, reflecting its triangular shape throughout the model evolution, whereas $K_p(t)$ changes significantly during the evolution of models that develop a low viscosity layer. The initial geometry of orogens is triangular ($K_p \sim 0.5$), and in some cases evolves to a double-triangle shape ($K_p \leq 0.4$; see Figs 11b and c at 30 Myr). When η_b is sufficiently small ($\sim 10^{20}$–10^{18} Pa s), the two peaks become balanced, with similar

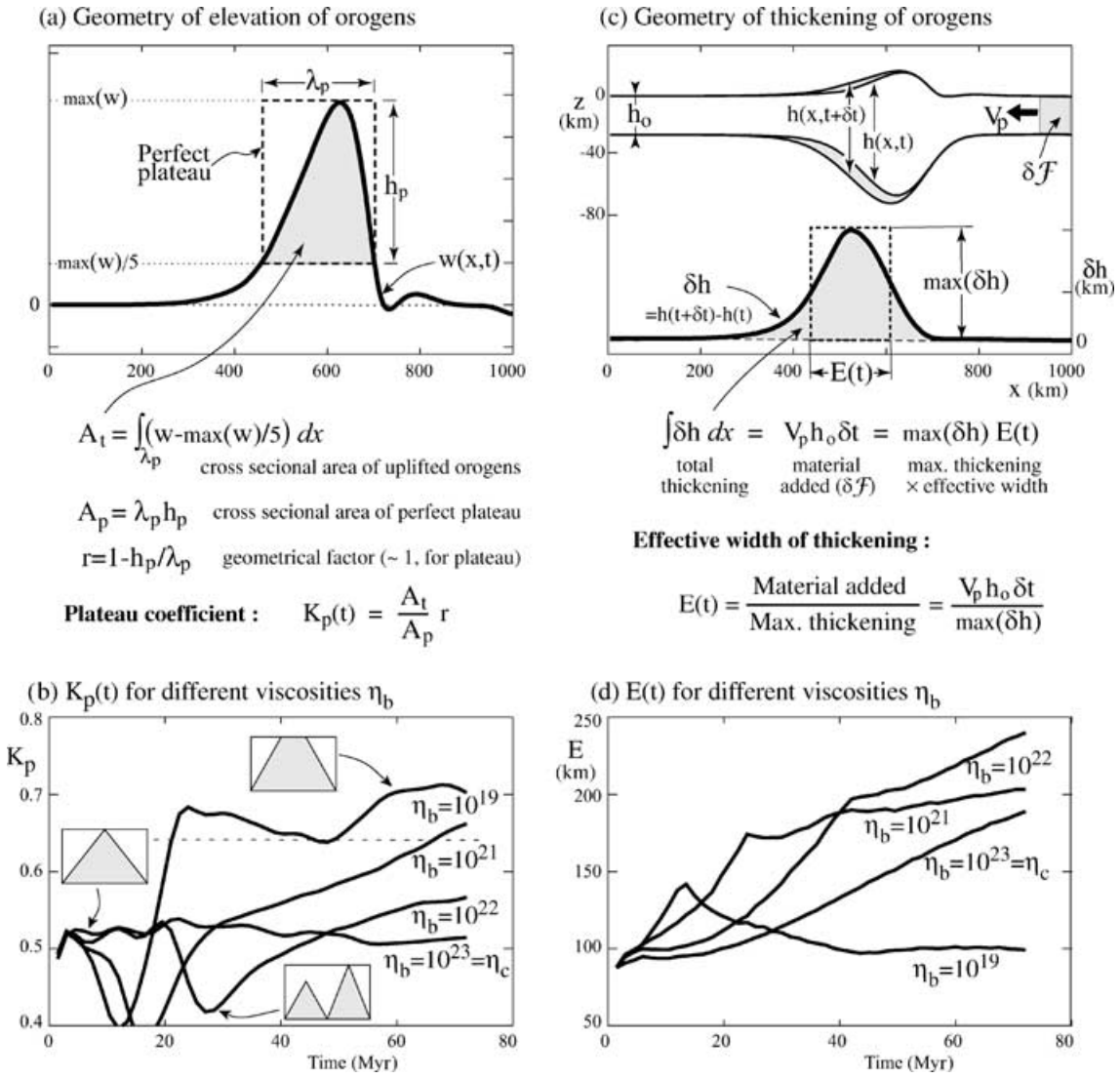

Figure A1. Definitions of $K_p(t)$ and $E(t)$ and examples of their evolution for variations on model V(23/n)z40 (depth-dependent viscosity with a step function in viscosity, $\eta_c = 10^{23}$ and $\eta_b = 10^n$, with the viscosity transition at depth $z^* = 40$ km; Table 2).

heights, and a plateau with no significant surface slope develops between them ($K_p > 0.65$, see details in Section 5.1).

A2 Dynamic characteristics: the effective width of thickening, $E(t)$

The effective width of thickening, $E(t)$, measures the distribution of crustal thickening as an orogen evolves, and reflects the size of the zone where the shape of the orogenic crust is actively changing (Fig. A1c). A rectangle with width E and height equal to the maximum thickening ($\delta h_{\max}$) is defined such that it has an area equal to the total change of thickness during time increment δt (grey area, Fig. A1c), and therefore equal to the flux of material added to the orogen during $\delta\, t$. During the growth of back-to-back wedges, $E(t)$ continues to increase with time. In contrast, during the growth of plateau where continued convergence is accommodated by widening of the model orogen rather than thickening, $E(t)$ reaches a constant value. Therefore the wedge/plateau transition is associated to the stabilization of $E(t)$ at a constant value (Fig. A1d).

Consideration of both $K_p(t)$ and $E(t)$ allows a more precise analysis of the general behaviour of orogens and provides simple measures for the transition from the growth of wedges to the growth of a plateau. An analysis of shape, $K_p(t)$ and $E(t)$ from many numerical models suggests that $K_p^* = 0.65$ can be used to indicate the onset of plateau-like behaviour.